

Using warm dust to constrain unseen planets

Amy Bonsor,¹★ Mark C. Wyatt,¹ Quentin Kral,¹ Grant Kennedy¹ ,^{2,3}
Andrew Shannon^{4,5} and Steve Ertel⁶

¹*Institute of Astronomy, University of Cambridge, Madingley Road, Cambridge CB3 0HA, UK*

²*Department of Physics, University of Warwick, Gibbet Hill Road, Coventry CV4 7AL, UK*

³*Centre for Exoplanets and Habitability, University of Warwick, Gibbet Hill Road, Coventry CV4 7AL, UK*

⁴*Department of Astronomy, Astrophysics, The Pennsylvania State University, State College, PA, USA*

⁵*Center for Exoplanets and Habitable Worlds, The Pennsylvania State University, State College, PA, USA*

⁶*Steward Observatory, Department of Astronomy, University of Arizona, 993 N. Cherry Ave, Tucson, AZ 85721, USA*

Accepted 2018 July 27. Received 2018 July 25; in original form 2018 June 18

ABSTRACT

Cold outer debris belts orbit a significant fraction of stars, many of which are planet hosts. Radiative forces from the star lead to dust particles leaving the outer belts and spiralling inwards under Poynting–Robertson drag. We present an empirical model fitted to N -body simulations that allows the fate of these dust particles when they encounter a planet to be rapidly calculated. High-mass planets eject most particles, whilst dust passes low-mass planets relatively unperturbed. Close-in, high-mass planets (hot Jupiters) are best at accreting dust. The model predicts the accretion rate of dust on to planets interior to debris belts, with mass accretion rates of up to hundreds of kilograms per second predicted for hot Jupiters interior to outer debris belts, when collisional evolution is also taken into account. The model can be used to infer the presence and likely masses of as yet undetected planets in systems with outer belts. The non-detection of warm dust with the Large Binocular Telescope Interferometer (LBTI) around Vega could be explained by the presence of a single Saturn mass planet, or a chain of lower mass planets. Similarly, the detection of warm dust in such systems implies the absence of planets above a quantifiable level, which can be lower than similar limits from direct imaging. The level of dust detected with LBTI around β Leo can be used to rule out the presence of planets more massive than a few Saturn masses outside of ~ 5 au.

Key words: planets and satellites: detection – planets and satellites: general – zodiacal dust – infrared: planetary systems.

1 INTRODUCTION

Many nearby stars have dusty analogues to our Solar system’s asteroid and Kuiper belt, observed in the infrared (see review by Wyatt 2008; Matthews & Kavelaars 2016). We observe small dust, which we know must be continuously replenished by collisions between larger parent bodies, as it has a short lifetime against collisions and radiative forces. Radiative forces from the star are strong enough to place the smallest grains on unbound or weakly bound orbits, as observed by the large haloes of debris systems such as Vega (Su et al. 2005; Sibthorpe et al. 2010), HR 4796 (Schneider et al. 2018) or HR 8799 (Matthews et al. 2014). Small dust grains that are large enough not to be blown out of the system can have their orbital velocities reduced by radiative forces, such that they gradually spiral inwards towards the star, under Poynting–Robertson drag (PR-drag). This

phenomenon is well understood theoretically (e.g. Burns, Lamy & Soter 1979), and has long been considered critical to the evolution of dust grains in the inner Solar system (e.g. Grün et al. 2001; Mann et al. 2006).

Dust spirals inwards from all outer debris belts due to PR-drag, but is generally depleted by mutual collisions before migrating far from its source (Wyatt 2005; van Lieshout et al. 2014; Kennedy & Piette 2015). Such a dust population has been suggested as an explanation for the mid-infrared excesses, resulting from warm dust, typically at ~ 1 au around Sun-like stars, found around some stars that also have far-infrared excesses from cold outer dust belts, typically at tens of au (Reidemeister et al. 2011; Mennesson et al. 2014; Kennedy & Piette 2015). Although suffering from a small number of detections, there is already a statistically significant link between mid- and far-infrared excesses (Mennesson et al. 2014; Ertel et al. 2018). Observations with the Large Binocular Telescope Interferometer (LBTI) find a 60 per cent occurrence rate for

* E-mail: amy.bonsor@gmail.com

mid-infrared excesses in systems with cold, outer dust belts, compared to 8 per cent in systems without far-infrared detections (Ertel et al. 2018). Even hotter dust is also observed closer in around some main-sequence stars in the near-infrared using interferometry, with instruments such as VLT/PIONIER or CHARA/FLUOR (Absil et al. 2013; Ertel et al. 2014). The link between such hot dust and cold, outer debris belts is less clear (Ertel et al. 2014) and an explanation for this hot dust remains elusive (Kral et al. 2017), although a mixture of scattering by comets (Bonsor, Augereau & Thébault 2012; Bonsor et al. 2014), a coupling of PR-drag and pile-up at the sublimation radius (Kobayashi et al. 2009; van Lieshout et al. 2014) and/or trapping in magnetic fields have been suggested (Rieke, Gáspár & Ballering 2016).

A growing number of planets are known to orbit interior to cold, outer debris belts (e.g. Marshall et al. 2014). These planets can have a significant influence on the population of dust in the inner planetary systems. Planets can eject or accrete dust. The Earth receives a significant flux of meteoroids, many of which originate in the asteroid belt and have spiralled inwards under PR-drag (Mann et al. 2004). Planets interior to debris discs may receive a similar flow of material, and their influence on the atmospheric dynamics of these planets is unknown. Characterization of the atmospheres of many close-in, massive planets has revealed the presence of dust or haze, which most likely is linked to internal atmospheric evolution, but could potentially have an external origin (Madhusudhan et al. 2016).

Following the evolution of dust particles from an outer debris belt to the inner regions of a planetary system is a complex problem, particularly in multi-planet systems. It is possible to make detailed models for our Solar system. These track the dynamical evolution of dust grains leaving the Kuiper belt (e.g. Liou, Zook & Dermott 1996), or known comets (e.g. Yang & Ishiguro 2018), using N -body simulations to track their interactions with the planets, taking into account the influence of non-gravitational forces, including radiative forces or stellar wind drag. Such simulations are computationally intensive, particularly for the massive grains that migrate the slowest, but contain the most mass. Collisional evolution is even harder to account for and, generally, is only considered using a statistical approach, which does not allow for consideration of interactions with planets (e.g. Reidemeister et al. 2011). Models that couple dynamics and collisions are computationally expensive to run (e.g. Stark & Kuchner 2009; Kral, Thébault & Charnoz 2013). Whilst it may be feasible to simulate individual systems, N -body simulations for the wide range of parameter space available to exoplanets would take a prohibitively long time. Instead this work aims to provide an alternate, fast to calculate, empirical means of calculating the fate of dust particles leaving a debris belt due to PR-drag. This enables it to be applied to the vast range of parameter space probed by exo-planetary systems.

The empirical fate of dust will be assessed using a simple analytic model, compared to the results of more computationally intensive N -body simulations. This will be used to calculate how much dust is present in inner planetary systems, including the Solar system and how much dust is accreted by planets. Moro-Martín & Malhotra (2005) performed N -body simulations for a similar problem, but focusing on the dust leaving the system, mainly ejected by planets. Their simulations had insufficient particle numbers to trace accretion on to planets. In this paper, we perform N -body simulations including sufficient particles to trace accretion by planets interior to debris belts, as well as ejection, as described in Section 2. We compare the results of these simulations to a simple analytic model, and present an empirical method to predict the fraction of particles

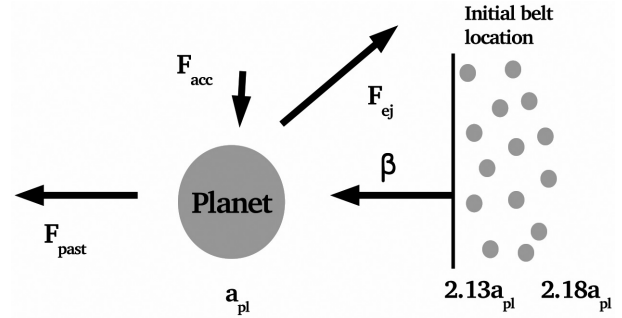


Figure 1. A schematic diagram of our approach, indicating the location of the initial belt in the N -body simulations which track the fraction of particles ejected by the planet (F_{ej}), the fraction accreted by the planet (F_{acc}) and the fraction that migrate past the planet, going on to hit the star (F_{past}), as described in Section 2.

that approach a planet migrating due to PR-drag that are accreted or ejected by the planet in Sections 3 and 4. This model is then used to make predictions for the mass accretion rates on to planets interior to outer debris belts (Section 5.1), to the Solar system (Section 5.2) and to predict the levels of dust in the inner regions of debris disc systems (Section 5.3), in relation to any planets that may orbit in these systems. We focus on two systems (Vega and β Leo) where LBTI observations provide important constraints on any planetary companions. Our conclusions are summarized in Section 6.

2 NUMERICAL SIMULATIONS

Numerical simulations are used to track the fate of particles leaving a debris belt and migrating inwards under PR-drag. We use the N -body code *Mercury* (Chambers 1999), with the addition of migration due to PR-drag and radiation pressure (Shannon, Mustill & Wyatt 2015). We use the *hybrid* integrator, which switches between the *symplectic* and *Burlisch-Stoer* integrators for close encounters. A single planet orbits interior to the dust belt, on a circular orbit, with semi-major axis, a_{pl} and mass, M_{pl} , around a star of mass $M_{\star} = 1 M_{\odot}$, as shown on the cartoon in Fig. 1. A belt of test particles start exterior to the planet. In order to speed up the simulations, we do not need to track the particle’s evolution from the outer belt all the way into the planet, instead we start the particles at between $2.13a_{pl}$ and $2.18a_{pl}$, outside the planet’s 3:1 resonance, where most dynamical interactions with the planet start. The particles migrate inwards at a rate specified by the ratio of the forces due to stellar radiation pressure to gravity, β , where

$$\beta = \frac{3L_{\star}Q_{PR}}{8\pi GM_{\star}\rho cD} \quad (1)$$

is the ratio of the force due to radiation pressure to the gravitational force on a particle of diameter D , density, ρ , around a star of luminosity, L_{\star} , and mass, M_{\star} . Q_{PR} is the radiation pressure efficiency factor, assumed to be 1 in this work, a valid approximation resulting from geometric optics for grains larger than $\sim 0.1 \mu\text{m}$, G and c are the gravitational constant and the speed of light, respectively. All variables are listed in Table A1.

The test particles all have low initial eccentricities of $e_i = 0.01$, either *low* or *moderate* initial inclinations, with $I_i = 0^{\circ}03$ and $I_i = 17^{\circ}$, and initial arguments of pericentre, longitudes of ascending node and free, true anomalies that are randomly selected. Low eccentricities when particles interact with the planet are likely given that significant migration under PR-drag will circularize orbits, although

we note here that for the highest values of β (fastest migration) there may not be sufficient time for orbits to be circularized. A time-step of $8 \left(\frac{a_{\text{pl}}}{\text{au}}\right)^{3/2}$ days is used.

The aim of the simulations is to track particles accreted by the planet. We, therefore, require that we have sufficient particles to resolve an accretion fraction of 0.3 per cent to 3σ , which assuming Poisson statistics and $\sigma = \sqrt{N}/N$ requires at least 3100 particles. The simulations were run until all particles have either been ejected, accreted by the planet or hit the central star. For each simulation we track the fraction ejected (F_{ej}), the fraction accreted by the planet (F_{acc}) and the fraction that migrate past the planet and go on to hit the star (F_{past}). The inner radius down to which the orbits of dust grains are followed is fixed at $a_{\text{pl}}/10$ in order to speed up the simulations. This is sufficient that particles are no longer under the influence of the planet, and unlikely to change their fate. The planet density is set to $\rho_{\text{pl}} = 5.52 \text{ g cm}^{-3}$ (Earth) for $M_{\text{pl}} < 30 M_{\oplus}$, i.e. rocky planets and $\rho_{\text{pl}} = 1.33 \text{ g cm}^{-3}$ (Jupiter) for $M_{\text{pl}} \geq 30 M_{\oplus}$, i.e. gas giants. The influence of changing the planet density is small.

A range of simulations were run varying the planet properties (a_{pl} and M_{pl}) and the migration rate (β). For a sub-set of the simulations, the stellar mass, M_* and inclination, I_i , were also changed. The results of all simulations are summarized in Tables A3 and A5 and Figs 2 and 3. The ejection rate is seen to increase steeply with planet mass, as seen by Moro-Martín & Malhotra (2005), ranging from no ejections to almost all particles ejected, for example for Earth mass to Jupiter mass planets at 10 au with $\beta = 0.1$. The same range in ejection rate is seen when varying semi-major axis at fixed planet mass, e.g. for $100M_{\oplus}$ no particles are ejected at 0.1 au and almost all particles are ejected at 100 au. Moro-Martín & Malhotra (2005) only saw an almost flat trend with semi-major axis, as they focused on higher planet masses and higher semi-major axes, where the ejection rate remains close to 1. The ejection rate falls off weakly for smaller particles (higher β), in a similar manner to that seen by Moro-Martín & Malhotra (2005). Fig. 3 shows that the accretion rate is almost always lower than the ejection rate, increasing only up to a maximum of about 20 per cent in these simulations. Accretion rates are highest for the highest mass planets, that are closest to the star, and accretion rates decrease with increasing β .

3 THE FATE OF PARTICLES THAT ENCOUNTER A PLANET

3.1 The model

The aim of this work is to provide an empirical means to predict the fraction of particles that spiral inwards under PR-drag towards a planet that is accreted, ejected and pass the planet, going on to hit the star, if no further planets are present. We base these predictions on the following simple analytic model. As in the numerical simulations, we only consider planets on circular orbits.

Consider the number of particles passing the planet, $N(t)$, to be reduced by both ejections and accretions at rates R_{ej} and R_{acc} per particle, respectively, i.e. where $1/R_{\text{acc}}$ is the mean time for any given particle to be accreted if it remained on its current orbit. If the initial number of particles is N_0 , and both rates are constant throughout the time the particles interact with the planet, and there are no further loss mechanisms, then:

$$\dot{N} = -R_{\text{acc}}N - R_{\text{ej}}N \quad (2)$$

$$N(t) = N_0 e^{-(R_{\text{acc}}+R_{\text{ej}})t}. \quad (3)$$

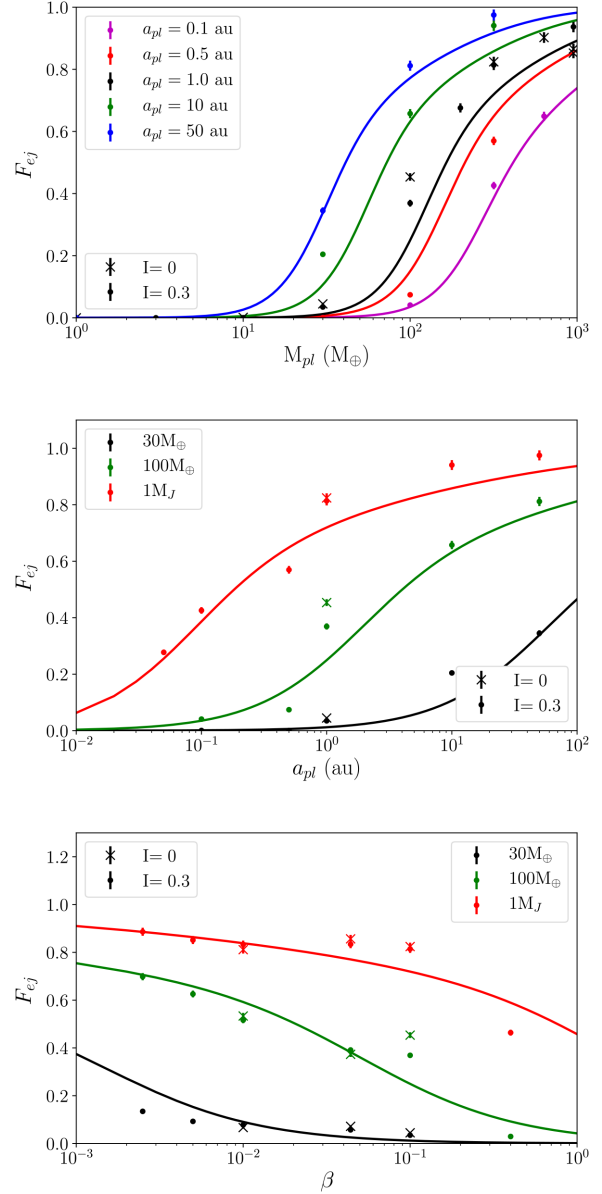


Figure 2. The results of the numerical simulations showing the fraction of particles ejected as a function of planet mass, for $\beta = 0.1$ (top panel), planet semi-major axis, for $\beta = 0.1$ (middle panel) and particle size, for $a_{\text{pl}} = 1 \text{ au}$ (β equation 1 bottom panel). The solid lines show a fit to the results of the form of equations (20) and (21), using the best-fitting parameters in Table 1. Error bars are 1σ , where $\sigma = \sqrt{N_{\text{ej}}}/N$.

The total number of particles ejected (N_{ej}) can then be calculated by integrating the rate of ejections over the time that the particle remains interacting with the planet, Δt , such that $N_{\text{ej}} = \int_0^{\Delta t} R_{\text{ej}} N(t) dt$, and the fraction ejected is

$$F_{\text{ej}} = \frac{N_{\text{ej}}}{N_0} = \frac{R_{\text{ej}}}{(R_{\text{acc}} + R_{\text{ej}})} (1 - e^{-(R_{\text{ej}}+R_{\text{acc}})\Delta t}). \quad (4)$$

In a similar manner, the number accreted, $N_{\text{acc}} = \int_0^{\Delta t} R_{\text{acc}} N(t) dt$, and the fraction accreted:

$$F_{\text{acc}} = \frac{N_{\text{acc}}}{N_0} = \frac{R_{\text{acc}}}{(R_{\text{acc}} + R_{\text{ej}})} (1 - e^{-(R_{\text{ej}}+R_{\text{acc}})\Delta t}). \quad (5)$$

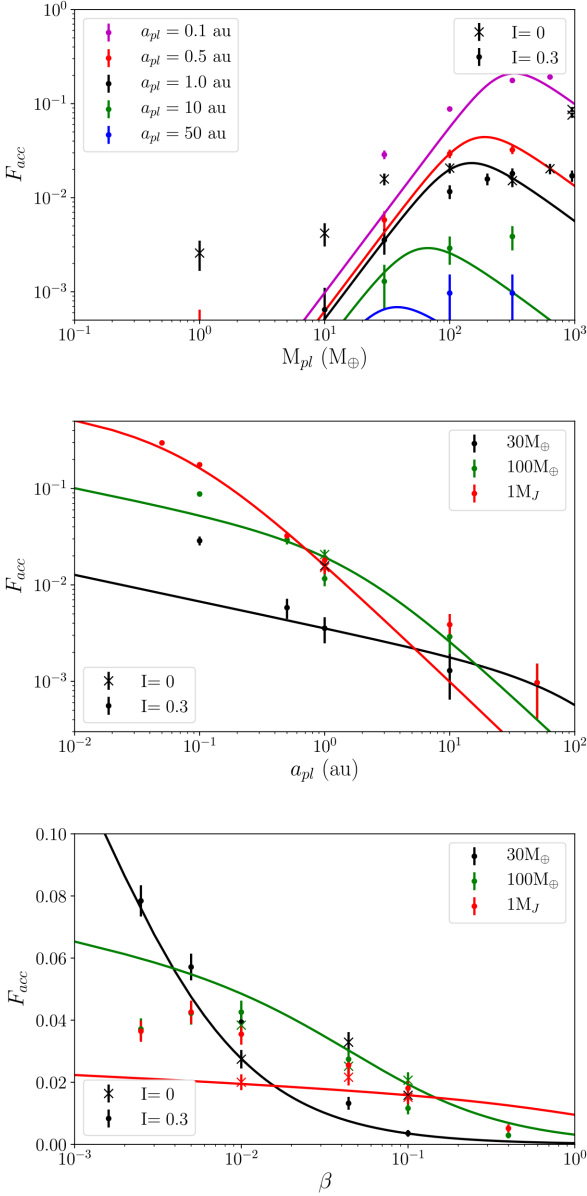


Figure 3. The results of the numerical simulations showing the fraction of particles accreted as a function of planet mass, for $\beta = 0.1$ (top panel), planet semi-major axis, for $\beta = 0.1$ (middle panel) and particle size, for $a_{\text{pl}} = 1$ au (β equation 1 bottom panel). The solid lines show a fit to the results of the form of equations (17) or (22) using the best-fitting parameters in Table 1. Error bars are 1σ , where $\sigma = \sqrt{N_{\text{acc}}/N}$.

The time that the particle remains under the potential influence of with the planet, Δt , is taken to be the time to traverse the planet-crossing region, migration from $a = a_{\text{pl}}(1 - e)$ to $a = a_{\text{pl}}(1 + e)$, where a , e are the orbital parameters of the particles, and a_{pl} is the semi-major axis of the planet. We now make the assumption that the particles are on almost circular orbits whilst migrating past the planet, which is a reasonable assumption as in general their eccentricity will have decayed following migration by PR-drag, except where β is high or the particles have migrated insufficient distance. We note here that the validity of this approximation may break down due to resonant interactions (see later). For almost circular orbits, the particle's semi-major axis decays under PR-drag

as (Wyatt & Whipple 1950; Burns et al. 1979; Shannon et al. 2015):

$$a_{\text{PR}} \approx -1.25 \left(\frac{M_{\star}}{M_{\odot}} \right) \left(\frac{a}{\text{au}} \right)^{-1} \beta + \mathcal{O}(e^2) \text{ au kyr}^{-1}. \quad (6)$$

Thus, the time to traverse the planet's orbit is given by:

$$\Delta t \approx \frac{1602}{\beta} \left(\frac{M_{\star}}{M_{\odot}} \right)^{-1} \left(\frac{a_{\text{pl}}}{\text{au}} \right)^2 e + \mathcal{O}(e^3) \text{ yr}. \quad (7)$$

The rate at which a particle interacts with the planet with a sufficiently small impact parameter such that it is accreted is given by:

$$R_{\text{acc}} = n \pi b_{\text{acc}}^2 v_{\text{rel}}, \quad (8)$$

where b_{acc} is the impact parameter required for accretion, v_{rel} the relative velocity between the particle and the planet, and n the density of colliders, given by $1/V_{\text{tor}}$, where the volume of the torus (V_{tor}) occupied by particles with semi-major axis, a , eccentricity, e , inclination, I and randomly distributed orbital elements is given by (Sykes 1990)

$$n = \frac{1}{V_{\text{tor}}} = \frac{1}{8\pi a^3 e \sin I} + \mathcal{O}(e^2). \quad (9)$$

The relative velocity between the planet and the particle, assuming that the particle is on an approximately circular orbit with $r = a_{\text{pl}}$, can be calculated by considering the velocity of a planet on a circular orbit, $v_{\text{K}}^2 = \frac{\mu}{a_{\text{pl}}}$, where $\mu = G M_{\star}$, and the velocity of a particle on a circular orbit that experiences gravity reduced by a factor $(1 - \beta)$:

$$v_{\text{pp}}^2 = v_{\text{K}}^2 (1 - \beta), \quad (10)$$

where the particle has approximately the planet's semi-major axis at the point of interaction. The planet's orbit is inclined by I relative to the particle, such that the planet's velocity is given by

$$\mathbf{v}_{\text{K}} = \begin{pmatrix} 0 \\ v_{\text{pl}} \cos I \\ v_{\text{pl}} \sin I \end{pmatrix} \quad (11)$$

and the particle's velocity:

$$\mathbf{v}_{\text{pp}} = \begin{pmatrix} 0 \\ v_{\text{pp}} \\ 0 \end{pmatrix}, \quad (12)$$

then

$$v_{\text{rel}}^2 = v_{\text{K}}^2 (2 - \beta - 2\sqrt{1 - \beta} \cos I). \quad (13)$$

If $\beta = 0$ this reduces to the standard expression in terms of the Tisserand parameter, T , $\frac{v_{\text{rel}}^2}{v_{\text{K}}^2} = 3 - T = 2(1 - \cos I)$.

The impact parameter for accretion is given by the planet's radius (R_{pl}) multiplied by a gravitational focusing factor, such that

$$b_{\text{acc}} = R_{\text{pl}} \sqrt{1 + \frac{v_{\text{esc}}^2}{v_{\text{rel}}^2}}, \quad (14)$$

where $v_{\text{esc}} = \sqrt{\frac{2GM_{\text{pl}}}{R_{\text{pl}}}}$ is the planet's escape velocity. For particles on nearly circular orbits, $v_{\text{rel}} \ll v_{\text{esc}}$, such that:

$$b_{\text{acc}} \approx \frac{R_{\text{pl}} v_{\text{esc}}}{v_{\text{rel}}} = 1.5 \times 10^{10} m \times \left(\frac{M_{\text{pl}}}{M_{\odot}} \right)^{2/3} \left(\frac{M_{\star}}{M_{\odot}} \right)^{-1/2} \times \left(\frac{\rho_{\text{J}}}{\rho_{\text{pl}}} \right)^{1/6} \left(\frac{a_{\text{pl}}}{\text{au}} \right)^{1/2} \left(\frac{v_{\text{K}}}{v_{\text{rel}}} \right). \quad (15)$$

All these expressions together lead to an accretion rate proportional to:

$$R_{\text{acc}} \Delta t = \alpha K_{\text{acc}} M_{\text{pl}}^{4/3} a_{\text{pl}}^{-1/2} M_{\star}^{-3/2} \beta^{-1}, \quad (16)$$

where the constant of proportionality, K_{acc} , depends only on the particle's orbital parameters when it interacts with the planet, the planet's density and is approximately independent of particle size (β). This simple model suggests a weak dependence on β resulting from the v_{rel} term in equations (13) and (15), which we ignore. In order to fit the simulation results we assume the form:

$$R_{\text{acc}} \Delta t = K_{\text{acc}} M_{\text{pl}}^{\alpha_a} a_{\text{pl}}^{\gamma_a} M_{\star}^{\delta_a} \beta^{\eta_a}. \quad (17)$$

The dependence of R_{acc} on planet mass, semi-major axis, particle size (β) and stellar mass are parametrized in terms of four parameters α_a , γ_a , η_a and δ_a , which will be determined empirically from fitting the simulation results. Equation (16) shows analytic predictions for their values, which are used to fix $\delta_a = -3/2$ as insufficient simulations were made to explore this parameter fully.

The rate of ejections can be determined in a similar manner. In this calculation, the cross-sectional area for ejections is given by $\pi(b_{\text{ej}}^2 - b_{\text{acc}}^2)$, where b_{ej} is the impact parameter for ejections. Whilst the impact parameter for ejection depends on the orientation of the interaction, here we assume that ejection occurs if the change in the particle's velocity due to the interaction $\Delta v > (\sqrt{2} + 1)v_K$.

Using Rutherford scattering to estimate Δv gives

$$\left(\frac{b_{\text{ej}}}{a_{\text{pl}}}\right) = \left(\frac{v_{K,\text{pl}}}{v_{\text{rel}}}\right)^2 \left(\frac{M_{\text{pl}}}{M_{\star}}\right) \left(\frac{4v_{\text{rel}}^2}{\Delta v^2} - 1\right)^{1/2}, \quad (18)$$

which is independent of β for $\beta \ll 1$, but again a weak dependence on β occurs due to the v_{rel} term, which becomes important for large β .

Combining these gives

$$R_{\text{ej}} \Delta t = n \pi (b_{\text{ej}}^2 - b_{\text{acc}}^2) v_{\text{rel}} \Delta t \approx K_{\text{ej}} a_{\text{pl}}^{1/2} M_{\text{pl}}^2 M_{\star}^{-5/2} \beta^{-1} - K_{\text{acc}} M_{\text{pl}}^{4/3} a_{\text{pl}}^{-1/2} M_{\star}^{-3/2} \beta^{-1}, \quad (19)$$

which we force to be always positive and model as

$$R_{\text{ej}} \Delta t = K_{\text{ej}} M_{\text{pl}}^{\alpha_e} a_{\text{pl}}^{\gamma_e} M_{\star}^{\delta_e} \beta^{\eta_e} - K_{\text{acc}} M_{\text{pl}}^{\alpha_a} a_{\text{pl}}^{\gamma_a} M_{\star}^{\delta_a} \beta^{\eta_a}. \quad (20)$$

Again, the four constants, K_{ej} , α_e , γ_e , η_e will be determined empirically from fitting the simulation results, whilst the stellar mass dependence, δ_e , is taken to be $-5/2$ from the analytics.

There are a number of reasons why this simple analytic model may not give a perfect match to the simulation results and an empirical model is required. For example, particles are scattered multiple times by the planet, and particles may become trapped in resonance prior to interacting with the planet, both of which lead to higher particle eccentricities and inclinations at interaction. In fact, analytic predictions suggest that trapping in the exterior 2:1 mean motion resonance is almost 100 per cent efficient for planets more massive than a few Earth masses (Shannon et al. 2015) for $\beta = 0.1$. Particles trapped in the 2:1 resonance evolve to eccentricities of around $(\frac{1}{5})^{1/2}$ before leaving the resonance. These factors are accounted for by allowing α , γ and η to vary from the analytic predictions.

Another factor to consider is the migration of particles scattered interior to the planet, which can quickly leave the influence of the planet, resulting in shorter interaction times than stated in equation (7). A significant number of particles are scattered inwards and migrate out of reach of the planet when the ejection rate is high. This tends to occur at high planet masses. Thus, to incorporate this in the empirical model, we add an additional parameter, ε , which

reduces the interaction time-scale, such that equations (4) and (5) become

$$F_{\text{ej}} = \frac{R_{\text{ej}}}{(R_{\text{acc}} + R_{\text{ej}})} \left(1 - e^{-\frac{(R_{\text{ej}} + R_{\text{acc}})\Delta t}{(1 + R_{\text{ej}}\Delta t)^\varepsilon}}\right), \quad (21)$$

$$F_{\text{acc}} = \frac{R_{\text{acc}}}{(R_{\text{acc}} + R_{\text{ej}})} \left(1 - e^{-\frac{(R_{\text{ej}} + R_{\text{acc}})\Delta t}{(1 + R_{\text{ej}}\Delta t)^\varepsilon}}\right). \quad (22)$$

In order to determine the values of the free parameters, we use a Markov chain Monte Carlo method (MCMC) to maximize the likelihood, using the EMCEE package of Foreman-Mackey et al. (2013), assuming a normal distribution, with errors on the number of particles ejected or accreted, given by $\sigma_{\text{ej}}(\mathbf{k}) = \frac{N_{\text{ej}}(\mathbf{k})^{1/2}}{N_0}$ and $\sigma_{\text{acc}}(\mathbf{k}) = \frac{N_{\text{acc}}(\mathbf{k})^{1/2}}{N_0}$, where N_{ej} and N_{acc} are the total number of particles ejected or accreted during the simulation and \mathbf{k} labels the set of simulation parameters (M_{pl} , a_{pl} and β) used. The likelihood function is given by

$$\ln \mathcal{L} = -2 \sum_{\mathbf{k}} \left(\frac{(F_{\text{ej}}(\mathbf{k})^{\text{model}} - F_{\text{ej}}(\mathbf{k})^{\text{sims}})^2}{\sigma_{\text{ej}}(\mathbf{k})^2} \right) - 2 \sum_{\mathbf{k}} \left(\frac{(F_{\text{acc}}(\mathbf{k})^{\text{model}} - F_{\text{acc}}(\mathbf{k})^{\text{sims}})^2}{\sigma_{\text{acc}}(\mathbf{k})^2} \right), \quad (23)$$

where $F_{\text{ej}}^{\text{model}}$ and $F_{\text{acc}}^{\text{model}}$ are the fraction of particles accreted and ejected in the model, derived from equations (4), (5), (21), and (22), and depend on the nine free parameters, K_{acc} , α_a , γ_a , η_a , K_{ej} , α_e , γ_e , η_e and ε . $F_{\text{ej}}^{\text{sim}}$ and $F_{\text{acc}}^{\text{sim}}$ are the number of particles ejected and accreted in the N -body simulations. Uniform priors are assumed for all free parameters.

Both the particle's initial eccentricity (e_i) and initial inclination (I_i) have the potential to influence the ability of planets to eject or accrete particles. Our best-fitting solution is determined based on a set of fiducial simulations in which $I_i = 0.3$ and $e_i = 0.01$; however, we made a few simple tests to show that these results are actually valid over a range of initial inclinations and initial eccentricities. This is because most particles are influenced by outer resonances with the planet before interacting and in fact, many particles are influenced by either the 2:1 mean-motion resonance or eccentricity-inclination resonances exterior to the planet, such that their inclinations and eccentricities evolve to similar values, irrespective of the initial values, before they interact with the planet. Simulations with $I_i = 0$ were performed for a sub-set of simulations with $a_{\text{pl}} = 1$ au and $\beta = 0.1$ (see Table A5 or Figs 2 and 3), and the difference between the fraction of particles ejected or accreted in the simulations compared to the empirical model was always less than 10 per cent. In a similar manner, simulations with $a_{\text{pl}} = 1$ au, $\beta = 0.1$ and $I_i = 0.3$ were performed for $e_i = 0.01$, $e_i = 0.1$ and $e_i = 0.4$ (see Table A4 and Fig. A1), and the difference between the fraction of particles ejected or accreted between the models was always less than 5 per cent. Very different behaviour was seen if eccentricities were increased above $e_i > 0.4$, which given this limited set of simulations suggests that the model may be valid up to eccentricities of around 0.4 as for such high eccentricities, i.e. above the maximum found in the 2:1 resonance, trapping probabilities and the ability of outer resonances to influence the particle's behaviour can be significantly different, and we deem that the empirical model presented here is no longer valid in this regime.

The posterior probability distribution of each parameter in the fit is shown in Fig. 4. Almost all walkers converge to a single best-fitting solution, although we note that as the model is limited and

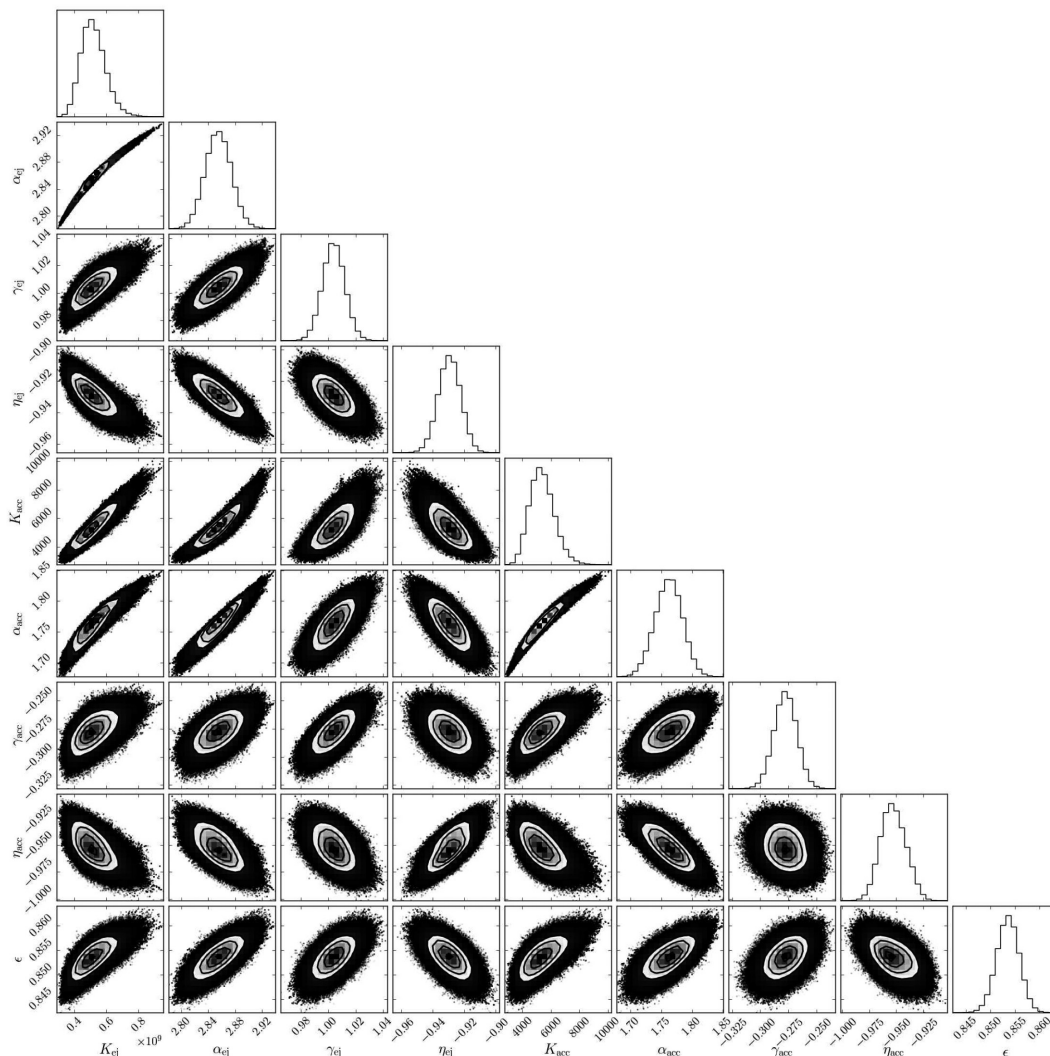


Figure 4. The posterior probability distributions of each parameter in the empirical fit to the ejections and accretions seen in the N -body simulations (equations 4, 17, 20), calculated by maximizing the likelihood (equation 23). Plot created using *corner* from Foreman-Mackey (2016).

Table 1. The analytic and numerical values of the constants in predicting the fraction of particles ejected of the form of equations (17), (20), (21) and (22).

Parameter	Dependence	Analytic	Numerical
K_{ej}			5.14×10^7
α_{ej}	M_{pl}	2	2.85
γ_{ej}	a_{pl}	1/2	1.00
η_{ej}	β	-1	-0.93
δ_{ej}	M_{\star}	-5/2	
K_{acc}			5350^{+900}_{-780}
α_{acc}	M_{pl}	4/3	1.76
γ_{acc}	a_{pl}	-1/2	-0.28
η_{acc}	β	-1	-0.95
δ_{acc}	M_{\star}	-3/2	
ε		0	0.85

unable to fit the data perfectly, alternative solutions may be equally valid. Our best-fitting parameters are listed in Table 1, and the best-fitting solutions are plotted as a function of planet mass, semi-major axis and particle size (β) in Figs 2 and 3.

3.2 Comparison between the model and the simulation results

Fig. 2 shows the fraction of particles ejected as a function of planet mass (top), semi-major axis (middle) and particle size or β (bottom). Solid lines show the best-fitting model, with parameters listed in Table 1, whilst the individual data points show simulation results. As discussed briefly in Section 2, the fraction of particles ejected increases with planet mass, which is explained by the analytics as being because larger planets can more readily impart a sufficiently large kick to eject particles. The model does a good job of reproducing the form of this behaviour, with the best-fitting exponent, α_{ej} varying by a small amount from the analytic prediction in order to achieve this (see Table 1). The parameter ε is critical in achieving the fit at large planet masses, where the fraction of particles ejected would otherwise tend to one. This is because some particles are scattered by long range interactions that are not quite sufficient to eject them, but can place them on orbits from where they quickly migrate inwards, out of reach of further interactions with the planet. Thus, the fraction of particles ejected is reduced due to the inclusion of the ε parameter for large ejection rates R_{ej} .

The fraction of particles ejected increases with semi-major axis, which the analytics show is predominantly because the

time-scale over which the particles interact with the planet increases (equation 7). Again the model produces a good fit to the observations, with the best-fitting exponent, γ_{ej} differing from the analytic prediction by a factor of ~ 2 (see Table 1). The fraction of particles ejected decreases for small particles (large β) that migrate quickly out of the region where they can interact with the planet. Our empirical model deviates slightly from the N -body simulations for large values of β . This can partly be attributed to an oversimplification in the model, which ignores a significant β dependence that is more complex than a power law, and contributes at high β .

Fig. 3 shows the fraction of particles accreted by a planet as a function of planet mass (top), semi-major axis (middle) and particle size or β (bottom). In general, as noted in Section 2, higher mass planets are better at accreting particles. However, for the largest planets, ejection becomes the dominant outcome (see top panel Fig. 2) and particles do not survive long enough to be accreted. Our model exhibits this behaviour due to the competition between the R_{acc} and R_{ej} terms in equations (21) and (22). At low planet mass, the model reduces to the behaviour demonstrated in equation (B2) of Wyatt et al. (1999), where accretion increases strongly with planet mass. However, for the lowest mass planets, e.g. Earth mass planets at 1 au, insufficient particles were included to follow accretion rates in detail. Such planets have lower probabilities to trap particles in outer resonances (Shannon et al. 2015) and thus the fate of particles is influenced more strongly by their initial parameters, as can be seen in Fig. 3 by the difference in accretion rates for the $I = 0$ and $I = 0.3$ simulations for low-mass planets.

The fraction of particles accreted by the planet decreases with the planet's semi-major axis (middle panel Fig. 3), which is explained by the analytics as the volume of the torus occupied by the particles (equation 9) increases faster with semi-major axis than the interaction time-scale (equation 7) and impact parameters (equation 14). The best-fitting model describes this behaviour successfully. The fraction of particles accreted by the planet decreases with β , as smaller particles migrate faster past the planet (bottom panel Fig. 3). The model does a reasonable job of fitting the dependence on β (particle size), although it is clear that this dependence is not strong and displays complexity beyond this simple model. This is expected, as the model (equations 17, 20, 21, and 22) misses out the complex dependence on β of the $\frac{v_{rel}}{v_K}$ term. Nonetheless, we deem that the model can make satisfactory predictions regarding the fraction of particles accreted. For ejections the difference between the model predictions and the simulation results is always less than a factor of 2, for accretions it is always less than a factor of 3, and for planet masses higher than $10M_{\oplus}$.

4 A MODEL FOR THE FATE OF PARTICLES THAT ENCOUNTER A PLANET

The model presented in Section 3 can be used to predict the average fate of particles spiralling inwards under PR-drag and whether they are accreted or ejected by any individual planet on a circular orbit using equations (17), (20), (21) and (22) and the best-fitting parameters from Table 1.

The fraction of particles predicted to be ejected (accreted) by a planet can be summarized in terms of the planet's semi-major axis and mass, as shown in Fig. 5 (Fig. 6). The red dots indicate all the known exo-planets. As expected, high-mass planets eject almost all particles they encounter, whereas low-mass planets eject almost no particles. A transition between ejection as the dominant outcome compared to accretion as the dominant outcome is expected to occur for planets where the Keplerian velocity is approximately equal to

the escape velocity (Wyatt et al. 2017), which is shown by the black solid line in Figs 5 and 6.

However, there is another criterion required for planets to eject particles; as for some planets, particles migrate past too fast for them to be ejected. This occurs for planets at large semi-major axis. Analytically we can estimate when this transition occurs by comparing the time-scale for particles to migrate past the planet due to PR-drag (equation 7) with the time-scale for the planet to eject particles. This is estimated by considering cometary diffusion, and the time-scale for this to lead to ejection, as derived in Tremaine (1993) (equation 3) and Brassier & Duncan (2008) (appendix A). Setting these two time-scales to be equal puts the transition from ejection to migration past the planet at

$$M_{pl, equal} = 830 M_{\oplus} \left(\frac{\beta}{e} \right)^{1/2} \left(\frac{M_{\star}}{M_{\odot}} \right)^{5/4} \left(\frac{a_{pl}}{\text{au}} \right)^{-1/4}, \quad (24)$$

where e is the particle's eccentricity. The dependence on eccentricity is small, and given that this is unknown, we set the eccentricity to a plausible value of $e = (\frac{1}{5})^{1/2}$, the eccentricity at which particles leave the 2:1 resonance (Shannon et al. 2015) to plot the dashed line in Fig. 5. This line separates the two regions of parameter space between where the dominant outcome is ejection and where the rate of ejection is low or negligible. Planets that lie above both the solid and dashed lines in Fig. 5 are best at ejecting particles.

In terms of accretion, Fig. 6 shows that significant accretion only occurs for planet masses below $v_K = v_{esc}$, noting the log-scale. However, for the lowest mass planets, particles migrate past the planet before they have time to be either accreted or ejected. The dotted line in Fig. 6 shows where the time-scale for accretion is equal to that for PR-drag, according to the empirical fit presented here, calculated by setting $R_{acc}\Delta t = 0.1$, using the model parameters shown in Table 1. Planets that are good at accreting particles lie above the dashed line and below the solid line in Fig. 6.

Fig. 7 shows the fraction of particles that are not lost in interactions with the planet. In general, whether or not particles are ejected dominates their fate and the fraction that hit the star, i.e. migrate past the planet without interacting, is very similar to the fraction that are not ejected. Thus, the dashed line, $t_{PR} = t_{scat}$, also explains this behaviour. The only exception to this is for planets where accretion is the dominant outcome which is at small semi-major axes and planet masses close to $M_{pl, equal}$. Particles that migrate past the planet are of interest as in multiple planet systems they are the particles that can go on to interact with other planets and may be the particles that make it into the inner regions to replenish an exozodiacal cloud.

4.1 Low-mass stars

Our numerical simulations focused on solar mass stars. However, we can use the analytic approximation to make a prediction for the dependence on stellar mass (equations 4 and 5). The analytic approximation calculates the fraction of particles ejected or accreted as a function of β , which for radiation pressure corresponds to the particle size. For such low-mass stars, however, it is questionable whether radiation pressure is sufficiently strong to lead to high values of β , and in fact, it has been suggested that forces due to the stellar wind may dominate (e.g. Augereau & Beust 2006). Nonetheless, we test the extension of the analytic model by a handful of numerical simulations, noting that care should be taken in applying this model to low-mass stars, particularly for the high values of β considered and the planet masses that may be a significant fraction of the stellar mass. For this suite of simulations the stellar mass was varied, for $M_{pl} = 100M_{\oplus}$, $\beta = 0.1$ and $a_{pl} = 1$ au and $M_{pl} = 1M_{\oplus}$,

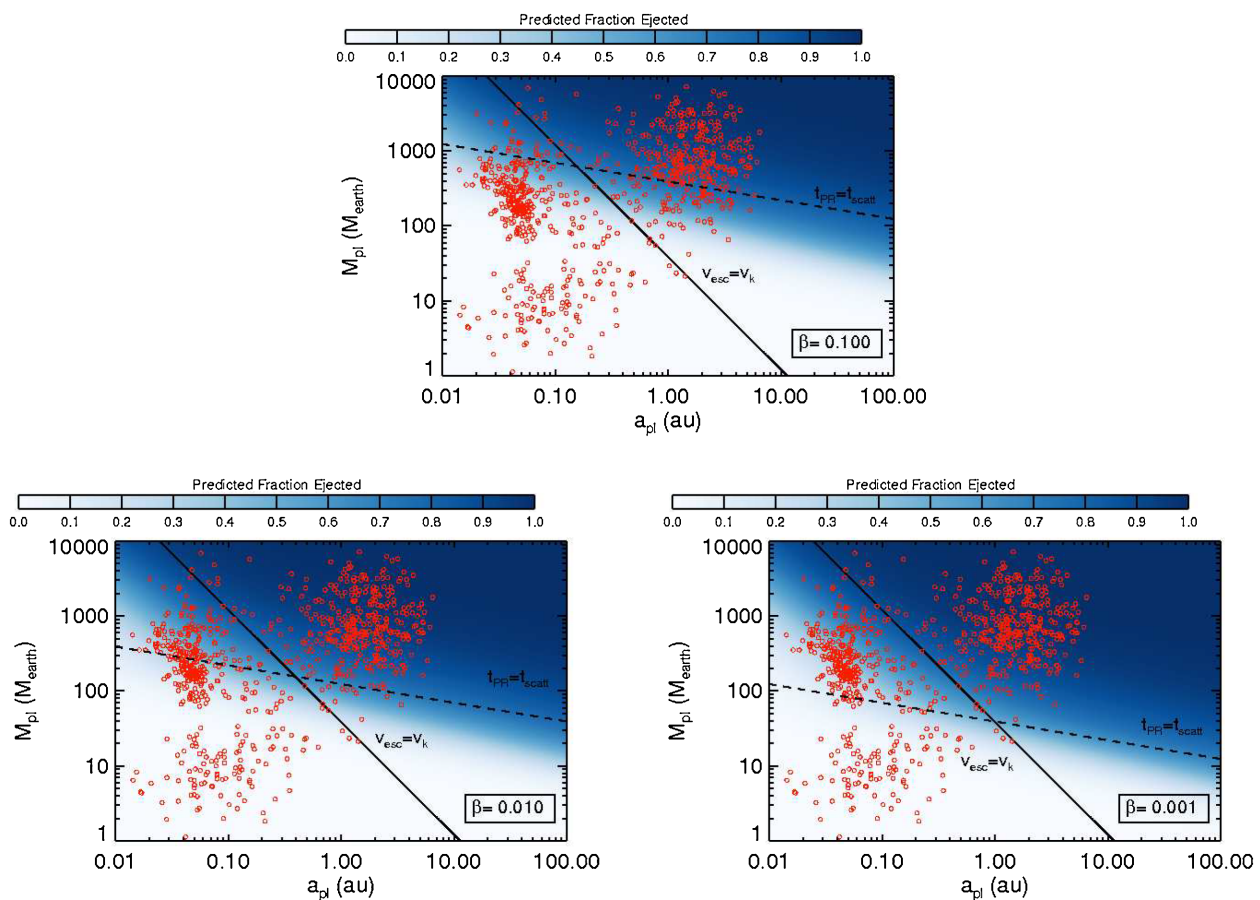


Figure 5. Predictions for the fraction of particles ejected by planets, as a function of the planet mass and semi-major axis, for $\beta = 0.1, 0.01, 0.001$, based on the best-fitting empirical model, calculated using equations (17), (20), (21) and (22) and parameters from Table 1. The solid line shows $v_K = v_{\text{esc}}$ and the dashed line shows where the time for the particles to migrate past the planet by PR-drag (equation 7) is equal to the time for particles to be ejected (equation 24).

$\beta = 0.1$ and $a_{\text{pl}} = 1$ au. The results of the numerical simulations, compared to the analytic predictions are shown in Fig. 8, based on equations (17) and (20) using $\delta_a = -3/2$ and $\delta_e = -5/2$. The simulations are by no means comprehensive and they indicate, as in a similar manner to the other parameters, an empirical fit to the numerical simulations might lead to slightly different values of δ_a and δ_e ; however, the analytically predicted values do a reasonably good job of predicting general trends as the stellar mass changes. The fraction of particles ejected increases for lower stellar masses, as does accretion, until the stellar mass is sufficiently low that ejection becomes the dominant outcome and planets are no longer as good at accreting, as seen in Fig. 8.

Fig. 9 shows predictions for the fraction of particles ejected and accreted, as a function of the planet’s semi-major axis and mass, for lower mass stars ($M_\star = 0.08 M_\odot$). A famous example of a multi-planet system around a low-mass star is the TRAPPIST-1, planetary system (Gillon et al. 2017). Most particles migrate past the TRAPPIST-1 planets. Our model predicts that for large grains, $\beta = 0.001$, $F_{\text{ej}} < 0.2$ per cent, and $F_{\text{acc}} < 10$ per cent, whereas for small grains e.g. $\beta = 0.1$, $F_{\text{ej}} < 10^{-3}$ per cent, and $F_{\text{acc}} \sim 0.1$ per cent. The TRAPPIST-1 planets are better at accreting than ejecting particles spiralling inwards due to PR-drag. However, a caveat is that test simulations for a TRAPPIST-1-like planet ($M_{\text{pl}} = 1M_\oplus$ at 0.01 au around a $0.08 M_\odot$ star) find accretion rates that are higher than predicted by the model (5 per cent for $\beta = 0.1$). This is likely due to a limitation in the model that does not always provide a good fit

for low-mass planets, particularly relevant at small semi-major axis (see the middle panel of Fig. 3), as noted in Section 4.2.

4.2 Limitations of the model

The model presented here is designed to be a fast alternative to detailed simulations, for predicting the fate of particles leaving a debris belt due to PR-drag. It does a reasonable job of reproducing the results of those simulations, within the limited parameter space tested. Clearly there are details of such simulations that the simple model misses. In particular, it does not do as good a job of reproducing the behaviour seen in simulations for large values of β (small dust grains). This is related to changes in the inclination and eccentricity distributions of particles at the point of interaction with the planet. The analytic model is derived assuming that eccentricities are low when particles interact with the planet, an approximation which may not be strictly valid following resonant interactions. Multiple interactions with the planet can increase eccentricities and inclinations in a manner not fully accounted for in the model. Another limitation regards accretion rates for low-mass planets, where in general the simulations were limited by the number of particles included and the fate of particles depends more strongly on their initial parameters. This is because resonant trapping is less efficient for low-mass planets. Clearly there are further subtleties related to the inclination/eccentricity distribution of particles as they interact with the planet that this simple model misses.

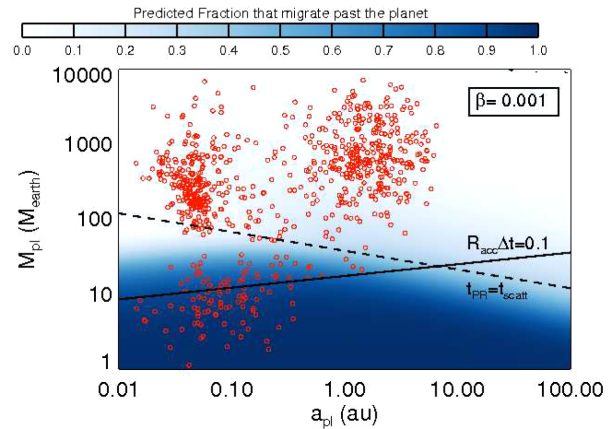
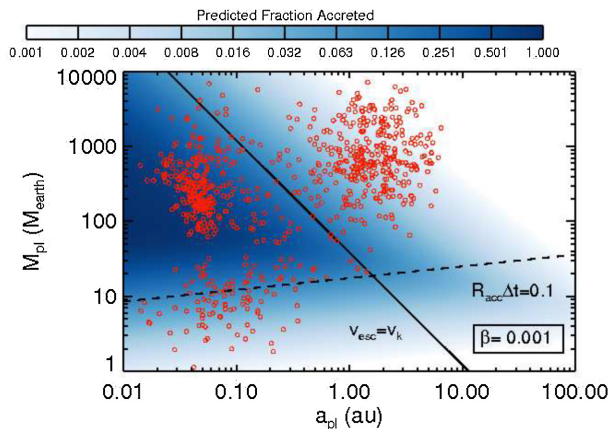
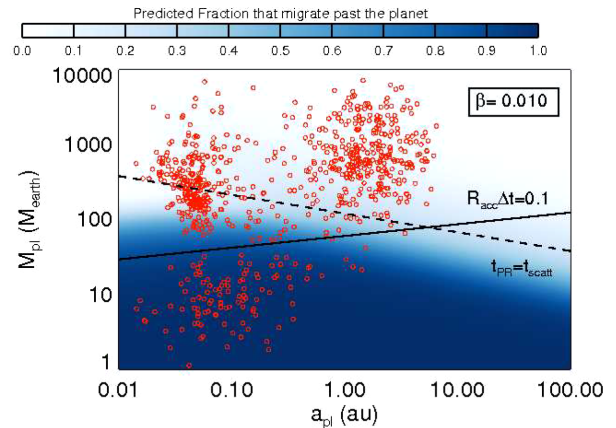
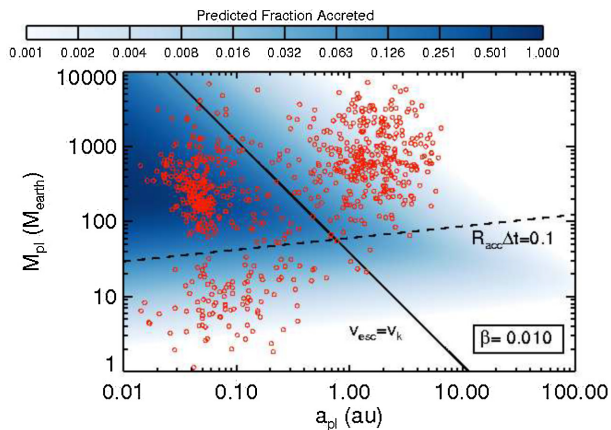
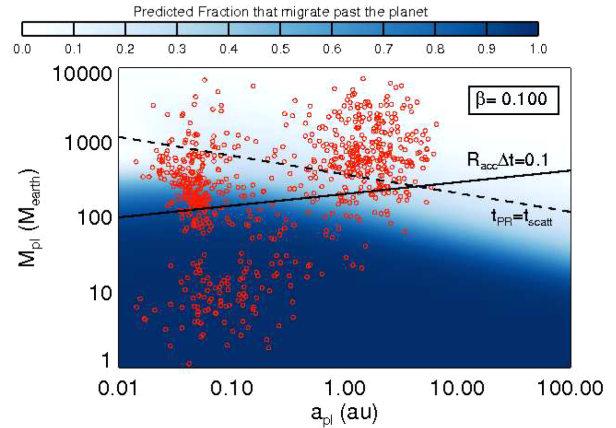
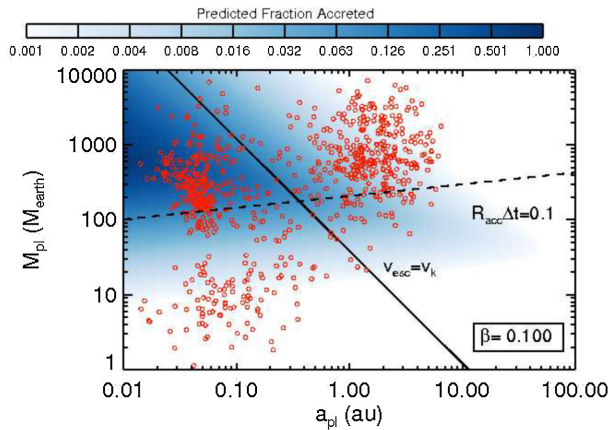


Figure 6. The same as Fig. 5, except for accretion. The dashed line shows where the time-scale for accretion is equal to that for PR-drag, according to the empirical fit presented here, calculated by setting $R_{\text{acc}} \Delta t = 1$ per cent.

For example, changes to the initial inclinations or eccentricities of particles at the start of simulations can change the fraction of particles ejected or accreted. In addition to which, the model only includes planets on circular orbits and the behaviour for planets on eccentric orbits may differ significantly. Another point to note is that the scaling with stellar mass presented here has not been robustly tested by simulations and is based purely on the analytic model.

Figure 7. The same as Fig. 5, except for the fraction of particles that migrate past a planet, suffering neither accretion nor ejection. The dashed line shows where the time for the particles to migrate past the planet by PR-drag (equation 7) is equal to the time for particles to be ejected (equation 24), and the solid line shows where the time-scale for accretion is equal to that for PR-drag, according to the empirical fit presented here, calculated by setting $R_{\text{acc}} \Delta t = 1$ per cent.

5 APPLICATIONS

The model presented here can be applied in multiple contexts, including predicting the mass accretion rates on to planets interior to outer debris belts, predicting the levels of dust in inner planetary systems, based on the architecture of the outer planetary system, and using observed levels of dust in the inner regions to predict the

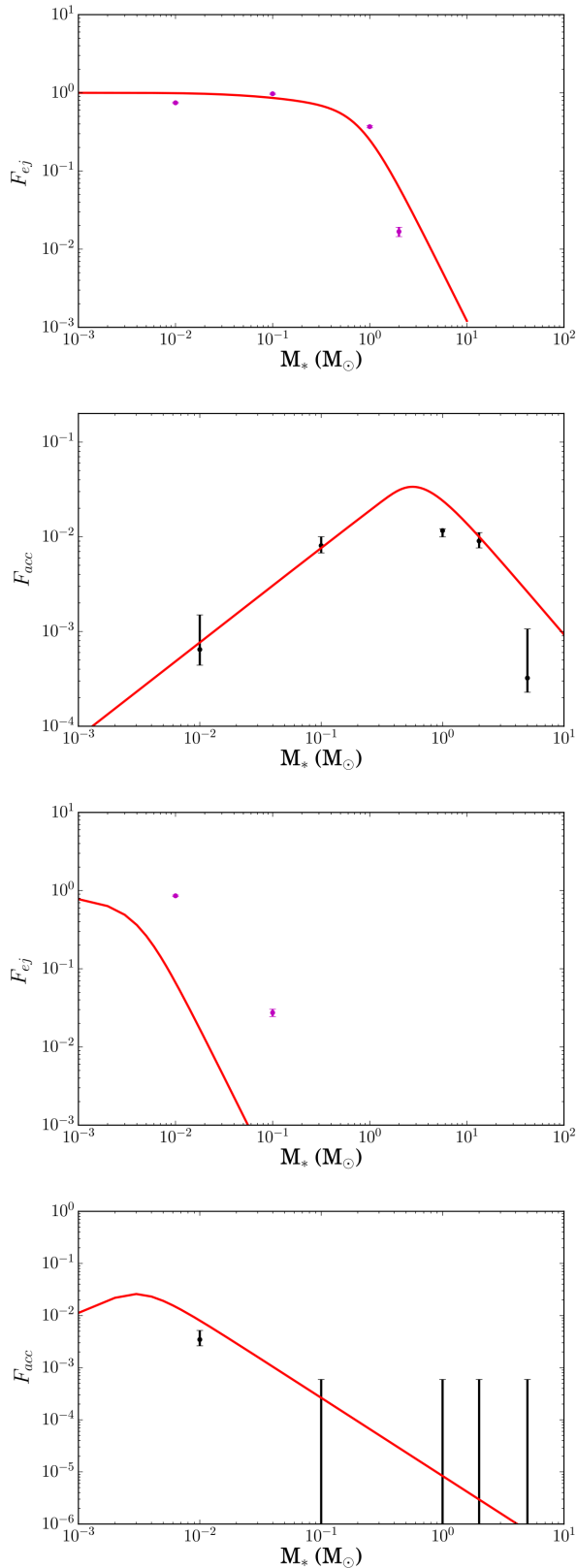


Figure 8. The fraction of particles ejected and accreted in the numerical simulations for $M_{\text{pl}} = 100M_{\oplus}$ (top two plots), $M_{\text{pl}} = 1M_{\oplus}$ (bottom two plots), $\beta = 0.1$ and $a_{\text{pl}} = 1$ au, varying stellar mass (M_*), compared to predictions, based on equations (17) and (20) using $\delta_a = 1/2$ and $\delta_e = -5/2$, as described in Section 4.1.

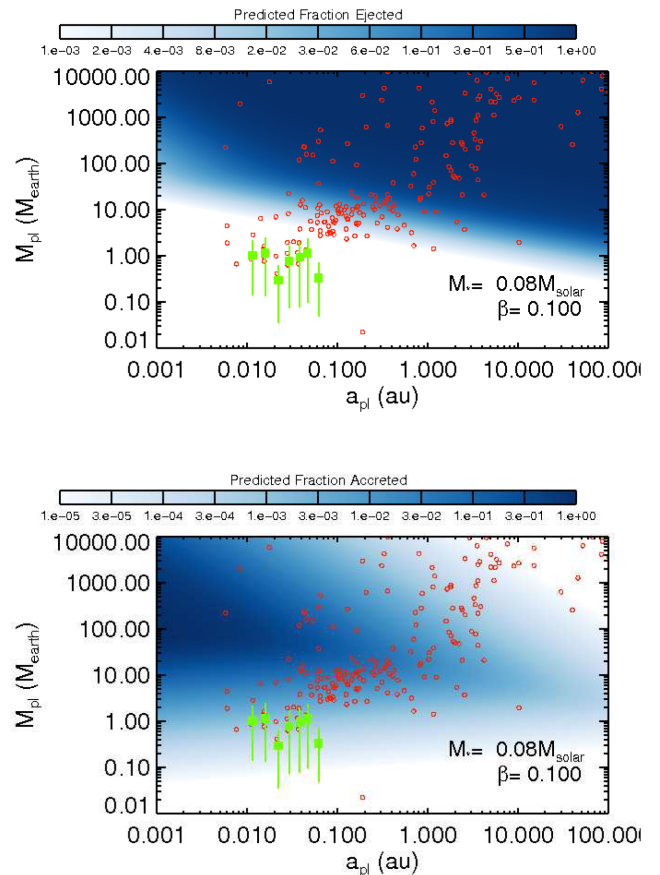


Figure 9. Predictions for the fraction of particles accreted and ejected by planets orbiting low-mass stars ($M_* = 0.08 M_{\odot}$) as a function of planet semi-major axis, a_{pl} and planet mass, M_{pl} . Over-plotted in red are exoplanets orbiting stars with $M_* < 0.5 M_{\odot}$ and as the green points, the TRAPPIST-1 planets (Gillon et al. 2017).

presence of outer planets. In this section we apply this model to a sub-set of observed systems in order to make predictions regarding the dust levels in their inner regions. The properties of these systems are listed in Table 2, which is limited to those with known outer debris belts and multiple planets orbiting interior to these belts listed in Marshall et al. (2014), or those with known outer belts and LBTI observations that characterize the levels of dust in the inner planetary system (Ertel et al. 2018).

The model presented here makes predictions regarding how the presence of planets changes the levels of dust leaving an outer belt due to PR-drag that reach the inner planetary system. Mutual collisions between these dust particles also play a critical role, but unfortunately are harder to model. For the purposes of this work, we rely on the simple model of Wyatt (2005) that traces the collisional evolution of a population of single size dust grains, to predict the depletion of dust due to collisions. We note, however, that collision rates could be higher (van Lieshout et al. 2014; Kennedy & Piette 2015) and that whether or not PR-drag is indeed the dominant transport mechanism to explain dust observed in the inner regions of planetary systems remains an open question (Kral et al. 2017).

In this simple model the effective optical depth (equivalent to the surface density of cross-sectional area) of the outer belt, $\tau(r_0)$, is

Table 2. The properties of a sample of planet-hosting debris discs, with the addition of Vega and β Leo. Planet data from Marshall et al. (2014) or exoplanet.eu. Fractional luminosities (f) of the outer belt are taken from Marshall et al. (2014) unless otherwise referenced. Radii are the inner edge of a resolved disc, where resolved imaging exists, otherwise, black-body radii from Marshall et al. (2014).

Name	L_* L_\odot	M_* M_\odot	Radius au	f 10^{-6}	a_{pl} au	M_{pl} M_J	e_{pl}
q ¹ Eri	1.52	1.11	85 ^a	405	2.022	0.93	0.16
τ Ceti	0.53	0.78	5 ^b	7.8	0.105, 0.195, 0.374, 0.552, 1.35	0.0063, 0.0098, 0.011, 0.014, 0.0208	0.16, 0.03, 0.08, 0.05
HD 19994	3.84	1.3	90	5.4	1.306	1.33	0.266
HD 20794	0.66	0.7	24 ^c	2.4	0.1207, 0.2036, 0.3498	0.0085, 0.0074, 0.015	0.0, 0.25
ϵ Eri	0.43	0.82	11 ^d	108	3.38	1.05	0.25
HD 40307	0.25	0.75	24	4.3	0.047, 0.08, 0.13	0.01291, 0.0211, 0.0281	0.0, 0
61 Vir	0.84	0.93	30 ^e	28	0.05006, 0.2169, 0.4745	0.0161, 0.0334, 0.0716	0.12, 0.14, 0.35
70 Vir	2.9	1.1	50	4.8	0.4836	7.46	0.4
GJ 581	0.012	0.31	25 ^f	91	0.04061, 0.0729, 0.2177, 0.02846	0.05, 0.017, 0.019, 0.0061	0.031, 0.07, 0.25, 0.32
HD 210277	1.0	1.09	155	5.1	1.131	1.273	0.476
HR 8799	5.4	1.47	145 ^g	49 ^h	14.5, 27.42, 9.68	9, 10, 10.7	–, 0.1, 0, 0
HD 82943	1.0	1.14	67 ⁱ	100 ^j	0.746, 1.19, 2.145	14.4, 14, 0.29	0.425, 0.203, 0
HD 69830	0.62	0.86	1 ^j	190	0.0186, 0.079, 0.63	0.165, 0.143, 0.253	0.1, 0.13, 0.07, 0.31, 0.33
β Leo	13.3	2.3	30 ^k	20			
Vega	57	2.9	85 ^l	19			

Notes. ^aLiseau et al. (2010), ^bLawler et al. (2014), ^cKennedy et al. (2015), ^dBooth et al. (2017), ^eMarino et al. (2017), ^fLestrade (2012), ^gBooth et al. (2016), ^hWyatt et al. (2007), ⁱKennedy et al. (2013), ^jSmith, Wyatt & Haniff (2009), ^kChurher et al. (2011) and ^lSibthorpe et al. (2010).

depleted at a distance r from the star as (equation 4 of Wyatt 2005)

$$\tau(r) = \frac{\tau(r_0)}{1 + 4\eta_0 \left(1 - \sqrt{\frac{r}{r_0}}\right)}, \quad (25)$$

where r_0 is the radius of the outer belt and $\eta_0 = \frac{5000}{\beta} \tau(r_0) \sqrt{\left(\frac{r_0}{\text{au}}\right) \left(\frac{M_\odot}{M_*}\right)}$. The effective optical depth of the outer belt, $\tau(r_0)$, can be related to the observed properties of the outer belt, including its fractional luminosity, f , radius, r and width, dr , assuming that all of the grains emit efficiently as black-bodies

$$\tau(r_0) = \frac{2 f r_0}{dr}. \quad (26)$$

For the radius of the outer belt, r_0 , we take the inner edge of the belt as determined from resolved imaging, where available and otherwise use the black-body radius determined from a black-body fit to the SED (Marshall et al. 2014). The belt width is generally undetermined or poorly constrained and therefore $dr = 0.1r_0$ is assumed for all systems. This assumption does not affect the conclusions significantly, since if the belt is broader, the assumption of a narrow belt supposes that the emission (fractional luminosity) comes from a narrow region, which, therefore, has a higher initial collision rate, such that the dust is ground down faster and the evolution, therefore, tends towards the same evolution as would have resulted from a broader belt. Moreover, changing dr from $0.1r_0$ to r_0 results in a < 10 per cent change in the effective optical depth at 1 au (for $r_0 = 200$ au). This is because the profile of $\tau(r)$ tends to a constant value for small radii and a change in the belt width only changes this constant value slightly. On the other hand, a significant change in the location of the belt can mean that we are no longer in the regime where $\tau(r)$ tends to a constant value, rather closer to the outer belt, where $\tau(r)$ can decrease steeply with r , such that for example changing $r_0 = 100$ au to $r_0 = 200$ au can produce changes in $\tau(1 \text{ au})$ of > 50 per cent.

In addition to this, this simple model may underestimate the rate of collisions based on the observed fractional luminosity, as in many cases the emission is dominated by small grains that are

inefficient in their emission at the relevant infrared wavelengths. The model is limited by the assumption of a single grain size and the lack of calibration against observations. The model of Wyatt (2005) would benefit from future updates to include multiple grain sizes (van Lieshout et al. 2014), and to allow grain size dependent sink terms, such as the ejection or accretion by planets presented here, as well as effects like resonant trapping (Shannon et al. 2015). The predictions made here can be readily updated to include any improved collision model, as available and would greatly benefit from any improvements.

5.1 Accretion on to planets interior to debris belts

Planets interior to outer debris discs can accrete dust that migrates inwards under PR-drag from the outer belt. The mass accretion rate due to PR-drag at a radius r , interior to a belt at r_0 , can be calculated by considering the density of particles migrating inwards and their velocity (van Lieshout et al. 2014) and is given by :

$$\dot{M}_{\text{PR}}(r) = F_{\text{acc}} \frac{Q_{\text{PR}} \tau(r) L_*}{c^2}, \quad (27)$$

where $\tau(r)$ is taken from equation (25) and F_{acc} is the fraction of material that passes a given planet that is accreted calculated using equation (5). The planets that are best at accreting PR dust are essentially hot Jupiters, with small semi-major axes and large planet masses, as shown by Fig. 6. Before looking at the accretion predicted for the planets in the systems with known debris from Table 2, we will first use Fig. 10 (top) to show how planet properties affect the predicted accretion rate. This shows the predicted mass accretion rates on to these planets, assuming that they orbit interior to a debris belt that lies at $r_{\text{belt}} = 200$ au with a fractional luminosity of $f = 10^{-5}$, around a solar luminosity star, the particles have $\beta = 0.1$ and any other planets that may exist in the system are ignored. This reinforces the expectation from Fig. 6 that close-in, high-mass planets accrete at the highest rates. Typical mass accretion rates for Jupiter mass planets orbiting at 0.01 au can be as high as hundreds of kilograms per second. The lower panel of Fig. 10 shows predictions for those systems with known debris belts and planets listed in

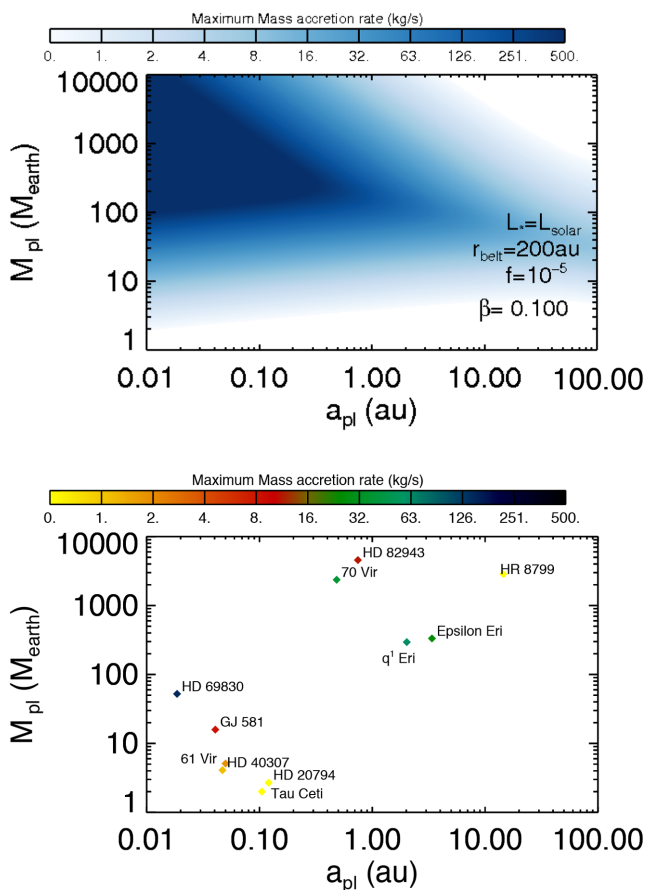


Figure 10. Predictions for the mass accretion rate of $\beta = 0.1$ dust grains on to planets interior to debris belts, calculated using equation (27). Top panel: for a typical outer debris belt with $r_{\text{belt}} = 200 \text{ au}$ and fractional luminosity $f = 10^{-5}$ around a solar mass star. Bottom panel: accretion rates on to the outer planet interior to those debris belt systems listed in Table 2.

Table 2. The highest accretion rates are predicted for systems like HD 69830 or HD 210277, which can be as high as hundreds of kilograms per second.

One of the aims of this work is to predict the amount of dust potentially accreted by planets interior to debris belts. The influence of this dust accretion on the atmospheres of these planets depends in a complex manner of the exact depth and temperature profile of the atmosphere, as well as how quickly the material sinks, how long the system has been accreting for and the primordial budget of similar species in the upper atmosphere.

It is interesting to note that in order to explain CO detections in the atmosphere of Saturn, a steady-state accretion of CO at a rate of $\sim 35 \text{ kg s}^{-1}$ is required (Cavalié et al. 2010), showing that the postulated levels of accretion can have an observable consequence. However, for Saturn, this CO is, instead, postulated to originate from the recent accretion of a cometary body (Cavalié et al. 2010). Indeed, Fig. 10 shows that such high-mass accretion rates (even assuming that the dust grains accreted had a generous CO mass fraction of e.g. 10 per cent) would not occur for planets like Saturn, instead, only for planets much closer to the star. The high temperatures of such planets result in a higher diffusivity of CO (Zahnle & Marley 2014) and therefore, much higher abundances of CO in the upper atmosphere would be expected naturally. Thus, for exoplanets, we do not necessarily expect that the accretion of material spiralling inwards from an outer debris belt via PR-drag could be detected in

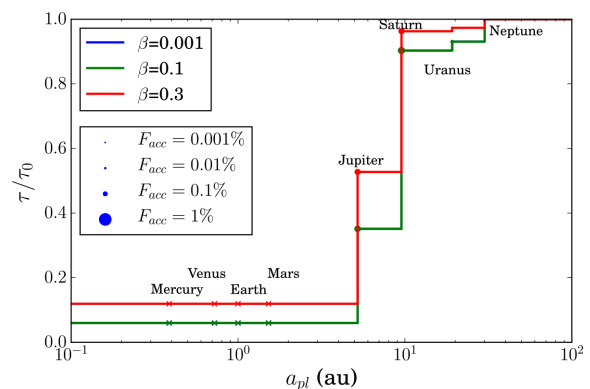


Figure 11. The change in effective optical depth of dust migrating inwards via PR-drag from the Kuiper belt, as it encounters the Solar system planets. The empirical model (equations 17, 20, 21 and 22) with best-fitting parameters from Table 1 is used to calculate the fraction of dust ejected or accreted by each planet in turn. Collisional depletion is ignored. The fraction of the dust that approaches each planet that is accreted is shown by the size of each marker at the position of each planet.

atmospheres with current instrumentation, but it may nonetheless play a role in the evolution of these planetary atmospheres that can be explored now that we are able to quantify the level of accretion expected.

5.2 Dust dragged in by PR-drag in the Solar system

In Fig. 11 we apply our model to the Solar system and calculate the fraction of dust leaving the Kuiper-belt due to PR-drag that is accreted, ejected and migrates past each planet from Neptune to Mercury. This ignores any collisional evolution in the dust population, as this will play a negligible role in low-density debris discs, like that in the Solar system (Vitense et al. 2012) and enables direct comparison with previous work. Both Neptune and Uranus lie in a regime where they eject a small fraction of the dust that migrates past them, depending on the speed at which it migrates (β). Saturn is better still at ejecting dust, and Jupiter is extremely efficient and ejects almost all the Kuiper belt dust that reaches it. None of the planets are very efficient at accreting dust, but the larger outermost planets can accrete of the order of a percent of the dust that approaches them. The model predicts that < 10 per cent of the dust leaving the Kuiper belt due to PR-drag reaches the inner Solar system and the terrestrial planets, with the highest fraction reaching the inner regions for the smallest particles (largest β).

The Solar system provides a good test case to compare the model presented here to other more detailed simulations. Based on N -body simulations considering a single planet, Vitense et al. (2012) predict similar levels of particles migrating past the planet, although clearly some differences exist, e.g. for $\beta = 0.259$. Vitense et al. (2012) find that for Neptune, Uranus, Saturn, 93 per cent, 95 per cent and 66 per cent of particles survive, compared to our model which finds 97 per cent 99 per cent and 52 per cent. For $\beta = 0.106$, Vitense et al. (2012) find 82 per cent, 80 per cent and 50 per cent which can be compared to 93 per cent, 97 per cent and 40 per cent from our model predictions. We note particularly that, as discussed in Section 4.2, the model is less valid for lower mass planets. The model presented here underpredicts the Kuiper belt dust grains that reach the inner Solar system compared to more detailed models of Liou et al. (1996) that use N -body simulations that consider solar radiation pressure, solar wind drag and gravitational interactions with the planets to

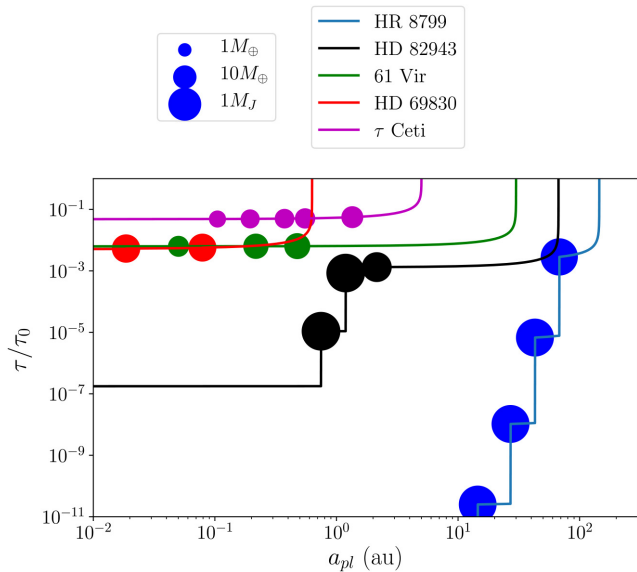


Figure 12. The change in effective optical depth of dust migrating inwards via PR-drag from known debris discs exterior to four example multi-planet systems. Planet properties are listed in Table 2. As the dust encounters each known planet in the system, both collisions (equation 25) and dynamical scattering (equation 21) are included, assuming $\beta = 0.1$.

find that 20 percent of Kuiper belt dust grains ($1\text{--}9\mu\text{m}$ or $\beta = 0.6\text{--}0.1$) evolve all the way to the Sun. This is to be compared with the < 10 percent of dust grains predicted by the empirical model presented here. The higher ejection rate by the giant planets that we predict could be related to the fact that our simulations did not include solar wind drag, or the importance of gravitational scattering by multiple planets, but is also partly expected from Fig. 2 which shows that we overpredict the ejection rate for high β ($\beta > 0.4$ small dust grains). This is because such small grains can be scattered inwards by an initial kick that is insufficient to eject them, but enables them to migrate quickly out of reach of the planet before a subsequent kick strong enough to eject them can occur. However, as noted earlier our predictions are accurate to within a factor of 3, even in the limit of small particles (large β), and we highlight again here an important advantage of this model is that it rapidly predicts the fate of PR-drag particles, even for large grains (small β), which are computationally expensive to simulate using N -body simulations.

5.3 Dust in inner planetary systems

The level of dust dragged in by PR-drag from an outer belt that reaches an inner planetary system depends on the collisional and dynamical evolution of the dust as it moves through the planetary system. The dynamical evolution of the dust depends strongly on the presence and orbits of planets interior to the outer belt. In particular in this work we have shown that massive planets, particularly those orbiting at small semi-major axis, can severely deplete the levels of dust dragged in by PR-drag that reach the inner planetary system (e.g. Fig. 7).

Using the simple model for collisional depletion (equation 25), alongside the model for dynamical depletion (equations 21 and 22), Fig. 12 shows predictions for the levels of depletion in the optical depth (surface density) interior to four example systems with known outer debris belts and known multiple planets, whose properties are

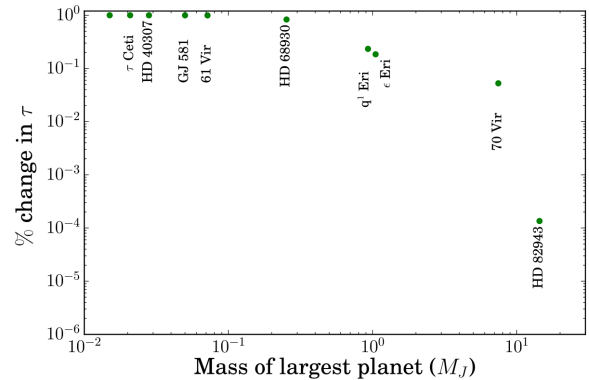


Figure 13. Predictions for the change in dust effective optical depth (surface density) at 0.01 au for the planet-hosting debris discs listed in Table 2 as a function of the highest mass planet in the system. Systems with high-mass planets i.e. HR 8799 predict a change in $\tau < 10^{-11}$ which falls below the axis limits of this plot.

listed in Table 2. The effective optical depth of dust is reduced by ejections and accretions as each planet is encountered. For systems with high-mass outer planets, such as HR 8799, most dust is ejected by the planets and the effective optical depth drops significantly before the inner regions, whereas for systems with close-in, lower mass planets such as 61 Vir or τ Ceti, dust levels remain close to those due to the depletion from mutual collisions.

Fig. 13 shows predictions for the level of depletion in the optical depth (surface density) of dust interior to those systems with known planets and debris discs listed in Table 2. This additional depletion due to the planets is plotted as a fraction of the optical depth in dust that would have been predicted at 0.01 au due to collisions alone (equation 25) and is plotted in Fig. 13 as a function of the mass of the largest known planet in each system. This shows that depletion is highest for those systems with the highest mass planets, although there is also a dependence on the location of those planets. Comparison of these model predictions with observations of dust in the inner regions of planetary systems with known outer belts can, therefore, be used to make predictions regarding the presence (absence) of further planets in these systems.

5.4 Using mid-infrared observations to predict planets

Both the LBTI and the Keck Interferometer Nuller (KIN) have been used to search for emission from dust in the inner regions, close to the habitable zones, around nearby stars (Mennesson et al. 2014; Defrère et al. 2015; Weinberger et al. 2015; Ertel et al. 2018). Many stars exhibit high levels of dust in the mid-infrared (Mennesson et al. 2014). A definitive explanation for this emission is not as yet clear; however, there is evidence that points towards the importance of dust leaving outer debris belts by PR-drag (Mennesson et al. 2014; Ertel et al. 2018), which could potentially be detectable in the mid-infrared (Kennedy & Piette 2015). There is a significantly higher incidence of mid-infrared excesses around stars with far-infrared excesses (cold, outer belts) (Mennesson et al. 2014; Ertel et al. 2018). High levels of dust in the near-infrared are also observed for many main-sequence stars using CHARA/FLUOR or VLT/PIONIER (Absil et al. 2013; Ertel et al. 2014). A good explanation for this dust, which is at levels much higher than expected due to PR-drag, is missing from the literature (Kral et al. 2017). We, therefore, focus the discussion here on warm dust, observed in the mid-infrared.

5.4.1 The absence of planets when exozodiacal dust is detected with LBTI

Dust in the inner regions of planetary systems with outer debris discs is inevitable as dust will always leak inwards due to PR-drag, and for many systems this dust will be detectable in the mid-infrared, even accounting for the collisional evolution. If massive planets orbit interior to the outer belt, these can significantly reduce the levels of dust reaching the inner regions. Thus, where dust is detected, if PR-drag is responsible for its presence, the model presented here can be used to rule out the presence of planets.

Specifically, we compare our models to LBTI observations at 11 μm , which probe regions at roughly 100–500 mas stellocentric separations. LBTI observes bright nearby main-sequence stars, so the angular scale corresponds to a few au, similar to the terrestrial planet region in the Solar system. To produce observables, we follow Kennedy et al. (2015) and Kennedy & Piette (2015) and take the absolute optical depth τ from the model for a given set of source belt and planet parameters, and assume $\beta = 0.1$ and a blackbody temperature law, to create a model of the disc surface brightness as a function of stellocentric radial distance. The disc model extends from radii interior to the LBTI inner working angle out to the source belt, though this extent does not influence the results because the inner disc is nulled by the observing technique, and the outer disc is too cool to contribute significant flux at 11 μm . This model is then attenuated by the LBTI transmission pattern to produce the disc flux observed when the star is ‘nulled’, and this flux is divided by the stellar flux to obtain the observable, the null depth.¹

LBTI observations of β Leo detect warm dust in the inner regions with a null depth of $1.16 \times 10^{-2} \pm 3.3 \times 10^{-3}$ (Ertel et al. 2018). Given its outer belt with an inner edge at 30 au with a fractional luminosity of 2×10^{-5} (Churcher et al. 2011), equation (25) can be used to predict the level of dust in the inner regions due to PR-drag. This dust would produce a predicted null depth that is 3σ below that observed if a planet more massive than the solid line in Fig. 14 orbited interior to the outer belt. Thus, if we assume that the PR-drag model is correct (i.e. the predicted null depth of 0.61 per cent in the no-planet case is correct), then planets more massive than Saturn between a few au and the outer belt can be ruled out. While the model in the no-planet case is consistent with the data at 2σ , further observations are needed to calibrate the PR-drag models so that future assertions about planet absence or presence can be made with confidence.

5.4.2 The planets that could explain the non-detection of exozodiacal dust with LBTI

For those systems with outer belts where no dust is detected in the inner regions with LBTI, it becomes relevant to ask how the dust levels were reduced to the observed levels. We postulate that the presence of planets that eject or accrete the dust before it reaches the inner regions could be responsible for the discrepancy and make predictions for the necessary properties of these planets.

To take Vega as an example, the presence of a bright, cold, outer belt would lead to dust in the inner planetary system. However, LBTI observations do not detect any dust (Ertel et al. 2018), giving

¹The null depth measured by LBTI is analogous to the disc/star flux ratio at 11 μm , with the difference that the disc flux is that transmitted through the LBTI transmission pattern (see Kennedy et al. 2015 for a full description).

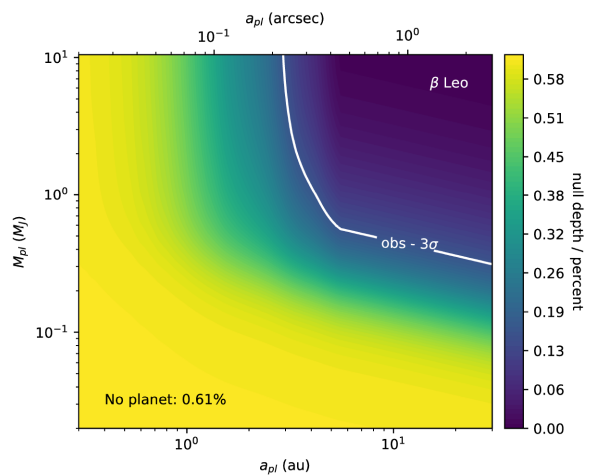


Figure 14. Contours showing the predicted null depths for LBTI observations of β Leo, based on the collisional evolution of dust spiralling inwards from the observed outer belt due to PR-drag and the presence of a single planet of given semi-major axis and mass. If the P-R drag model is correct and no planet orbits β Leo, the predicted null depth is 0.61 per cent. Planets above the solid lines would remove sufficient dust spiralling inwards due to PR-drag that the predicted null depth with LBTI would be 3σ below those observed (Ertel et al. 2018) (see discussion in Section 5.4).

an observed null depth of $2.4 \times 10^{-3} \pm 1.5 \times 10^{-3}$.² Given the observed outer belt at 85 au, with a fractional luminosity of 1.9×10^{-5} (Wyatt et al. 2007; Sibthorpe et al. 2010), reduced by collisions using equation (25) and accretion and ejection by a single planet, Fig. 15 shows the predicted null depths as a function of the planet’s mass and semi-major axis. The observed null depth, including a 3σ error, is consistent with the predictions of the PR-drag model, without the need to invoke the presence of any planets. However, if we take the observed null depth at face value (0.24 per cent), the presence of a single Saturn mass planet at around ~ 10 au could reduce the predicted flux (0.31 per cent) arriving from the outer belt to the observed (0.24 per cent), assuming the PR-drag model is correct. While the model in the no-planet case is consistent with the data at 2σ , further observations are needed to calibrate the PR-drag models so that future assertions about planet absence or presence can be made with confidence.

6 CONCLUSIONS

- (i) We present a simple empirical model for calculating the fate of dust leaving a debris disc and migrating inwards under PR-drag when it encounters a planet.
- (ii) The model enables the fate of dust to be calculated rapidly, avoiding the need for computationally intensive simulations; in particular it predicts the fraction of particles accreted or ejected by a planet, as a function of the planet properties.
- (iii) The model considers planets on circular orbits, and predicts the rate at which dust particles spiralling inwards under PR-drag are ejected and accreted (equations 17 and 20):

$$R_{\text{acc}} \Delta t = K_{\text{acc}} M_{\text{pl}}^{\alpha_a} a_{\text{pl}}^{\gamma_a} M_{\star}^{\delta_a} \beta^{\eta_a}$$

$$R_{\text{ej}} \Delta t = K_{\text{ej}} M_{\text{pl}}^{\alpha_e} a_{\text{pl}}^{\gamma_e} M_{\star}^{\delta_e} \beta^{\eta_e} - K_{\text{acc}} M_{\text{pl}}^{\alpha_a} a_{\text{pl}}^{\gamma_a} M_{\star}^{\delta_a} \beta^{\eta_a}.$$

²New LBTI observations for Vega indicate that an update is required to this model, which will be included in future work, but were not available in sufficient time to include in this work.

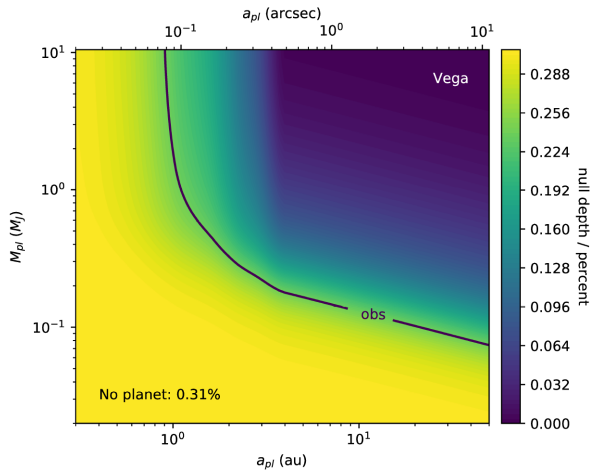


Figure 15. Contours showing the predicted null depths for LBTI observations of Vega, based on the collisional evolution of dust spiralling inwards from the observed outer belt due to PR-drag and the presence of a single planet of given semi-major axis and mass. If the PR drag model is correct and no planet orbits Vega, the predicted null depth is 0.31 per cent. The observed null depth, including a 3σ error, is consistent with the predictions of the PR-drag model, without the need to invoke the presence of any planets. However, if we take the observed null depth at face value, the presence of a single planet above the solid line could reduce the predicted flux (0.31 per cent) arriving from the outer belt to that observed (0.24 per cent) (Ertel et al. 2018) (see discussion in Section 5.4).

with best-fitting parameters listed in Table 1, which are used to determine the fraction of particles accreted or ejected by a planet (equations 21 and 22):

$$F_{\text{ej}} = \frac{R_{\text{ej}}}{(R_{\text{acc}} + R_{\text{ej}})} \left(1 - e^{-\frac{(R_{\text{ej}} + R_{\text{acc}})\Delta t}{(1 + R_{\text{ej}}\Delta t)^e}} \right)$$

$$F_{\text{acc}} = \frac{R_{\text{acc}}}{(R_{\text{acc}} + R_{\text{ej}})} \left(1 - e^{-\frac{(R_{\text{ej}} + R_{\text{acc}})\Delta t}{(1 + R_{\text{ej}}\Delta t)^e}} \right).$$

(iv) This model shows that most particles are ejected by high-mass planets, particularly at large semi-major axis, where the time-scale for ejection is shorter than the PR-drag time-scale (equation 7) (see Section 4).

(v) Ejection is the dominant outcome for planets where the Keplerian velocity is significantly smaller than the escape velocity ($v_K \ll v_{\text{esc}}$) and the time-scale for particles to be scattered is shorter than the time-scale for them to migrate past the planet (equation 24).

(vi) This model shows that high-mass, close-in planets, i.e. hot Jupiters, are best at accreting dust dragged in by PR-drag and can be used to predict the rate at which such planets accrete dust.

(vii) In multi-planet systems, the presence or absence of dust interior to a chain of planets with an outer debris disc provides clues as to the presence (or absence) of as yet undetected massive planets in the planetary system.

(viii) LBTI detections rule out the presence companions with masses greater than a few Saturn mass outside of ~ 5 au for β Leo, whilst the non-detection of warm dust for Vega could be explained by the presence of a single Saturn mass planet, or a chain of lower mass planets, orbiting interior to the outer belt.

ACKNOWLEDGEMENTS

We thank Philippe Thebault for his useful referee comments which greatly improved the quality of the manuscript. Discussions with

Jeremy Leconte, Alan Jackson, Sebastian Marino and the initial part III project of B. A. Greenwood-Rogers were of great benefit to this work. AB acknowledges a Royal Society Dorothy Hodgkin Fellowship. AS is partially supported by funding from the Center for Exoplanets and Habitable Worlds. The Center for Exoplanets and Habitable Worlds is supported by the Pennsylvania State University, the Eberly College of Science, and the Pennsylvania Space Grant Consortium. GMK is supported by the Royal Society as a Royal Society University Research Fellow.

REFERENCES

- Absil O. et al., 2013, *A&A*, 555, A104
 Augereau J.-C., Beust H., 2006, *A&A*, 455, 987
 Bonsor A., Augereau J.-C., Thébault P., 2012, *A&A*, 548, A104
 Bonsor A., Raymond S. N., Augereau J.-C., Ormel C. W., 2014, *MNRAS*, 441, 2380
 Booth M. et al., 2016, *MNRAS*, 460, L10
 Booth M. et al., 2017, *MNRAS*, 469, 3200
 Brassier R., Duncan M. J., 2008, *Celest. Mech. Dyn. Astron.*, 100, 1
 Burns J. A., Lamy P. L., Soter S., 1979, *Icarus*, 40, 1
 Cavalié T. et al., 2010, *A&A*, 510, A88
 Chambers J. E., 1999, *MNRAS*, 304, 793
 Churcher L. J. et al., 2011, *MNRAS*, 417, 1715
 Defrère D. et al., 2015, *ApJ*, 799, 42
 Ertel S. et al., 2014, *A&A*, 570, A128
 Ertel S. et al., 2018, *AJ*, 155, 194
 Foreman-Mackey D., 2016, Scatterplot matrices in python, J. Open Source Software, 24
 Foreman-Mackey D., Hogg D. W., Lang D., Goodman J., 2013, *PASP*, 125, 306
 Gehrels N., 1986, *ApJ*, 303, 336
 Gillon M. et al., 2017, *Nature*, 542, 456
 Grün E., Gustafson B. A. S., Dermott S., Fechtig H., 2001, Interplanetary dust, Astronomy and Astrophysics Library, Springer, Berlin
 Kennedy G. M., Piette A., 2015, *MNRAS*, 449, 2304
 Kennedy G. M., Wyatt M. C., Bryden G., Wittenmyer R., Sibthorpe B., 2013, *MNRAS*, 436, 898
 Kennedy G. M. et al., 2015, *ApJS*, 216, 23
 Kennedy G. M. et al., 2015, *MNRAS*, 449, 3121
 Kobayashi H., Watanabe S.-i., Kimura H., Yamamoto T., 2009, *Icarus*, 201, 395
 Kral Q., Thébault P., Charoz S., 2013, *A&A*, 558, A121
 Kral Q. et al., 2017, *Astron. Rev.*, 13, 69
 Lawler S. M. et al., 2014, *MNRAS*, 444, 2665
 Lestrade J.-F. et al., 2012, *A&A*, 548, A86
 Liou J.-C., Zook H. A., Dermott S. F., 1996, *Icarus*, 124, 429
 Liseau R. et al., 2010, *A&A*, 518, L132
 Madhusudhan N., Agúndez M., Moses J. I., Hu Y., 2016, *Space Sci. Rev.*, 205, 285
 Mann I. et al., 2004, *Space Sci. Rev.*, 110, 269
 Mann I., Köhler M., Kimura H., Cechowski A., Minato T., 2006, *A&AR*, 13, 159
 Marino S., Wyatt M. C., Kennedy G. M., Holland W., Matrà L., Shannon A., Ivison R. J., 2017, *MNRAS*, 469, 3518
 Marshall J. P. et al., 2014, *A&A*, 565, A15
 Matthews B. C., Kavelaars J., 2016, *Space Sci. Rev.*, 205, 213
 Matthews B., Kennedy G., Sibthorpe B., Booth M., Wyatt M., Broekhoven-Fiene H., Macintosh B., Marois C., 2014, *ApJ*, 780, 97
 Mennesson B. et al., 2014, *ApJ*, 797, 119
 Moro-Martín A., Malhotra R., 2005, *ApJ*, 633, 1150
 Reidemeister M., Krivov A. V., Stark C. C., Augereau J., Löhne T., Müller S., 2011, *A&A*, 527, A57
 Rieke G. H., Gáspár A., Ballering N. P., 2016, *ApJ*, 816, 50
 Schneider G. et al., 2018, *AJ*, 155, 77
 Shannon A., Mustill A. J., Wyatt M., 2015, *MNRAS*, 448, 684

- Sibthorpe B. et al., 2010, *A&A*, 518, L130
 Smith R., Wyatt M. C., Haniff C. A., 2009, *A&A*, 503, 265
 Stark C. C., Kuchner M. J., 2009, *ApJ*, 707, 543
 Su K. Y. L. et al., 2005, *ApJ*, 628, 487
 Sykes M. V., 1990, *Icarus*, 85, 267
 Tremaine S., 1993, in Phillips J. A., Thorsett S. E., Kulkarni S. R., eds, ASP Conf. Ser. Vol. 36, Planets Around Pulsars. The Distribution of Comets Around Stars. Astron. Soc. Pac., San Francisco, p. 335
 van Lieshout R., Dominik C., Kama M., Min M., 2014, *A&A*, 571, A51
 Vitense C., Krivov A. V., Kobayashi H., Löhne T., 2012, *A&A*, 540, A30
 Weinberger A. J. et al., 2015, *ApJS*, 216, 24
 Wyatt M. C., 2005, *A&A*, 433, 1007
 Wyatt M. C., 2008, *ARA&A*, 46, 339
 Wyatt S. P., Whipple F. L., 1950, *ApJ*, 111, 134
 Wyatt M. C., Dermott S. F., Telesco C. M., Fisher R. S., Grogan K., Holmes E. K., Piña R. K., 1999, *ApJ*, 527, 918
 Wyatt M. C., Smith R., Su K. Y. L., Rieke G. H., Greaves J. S., Beichman C. A., Bryden G., 2007, *ApJ*, 663, 365
 Wyatt M. C., Bonsor A., Jackson A. P., Marino S., Shannon A., 2017, *MNRAS*, 464, 3385
 Yang H., Ishiguro M., 2018, *ApJ*, 854, 173
 Zahnle K. J., Marley M. S., 2014, *ApJ*, 797, 41

APPENDIX A :

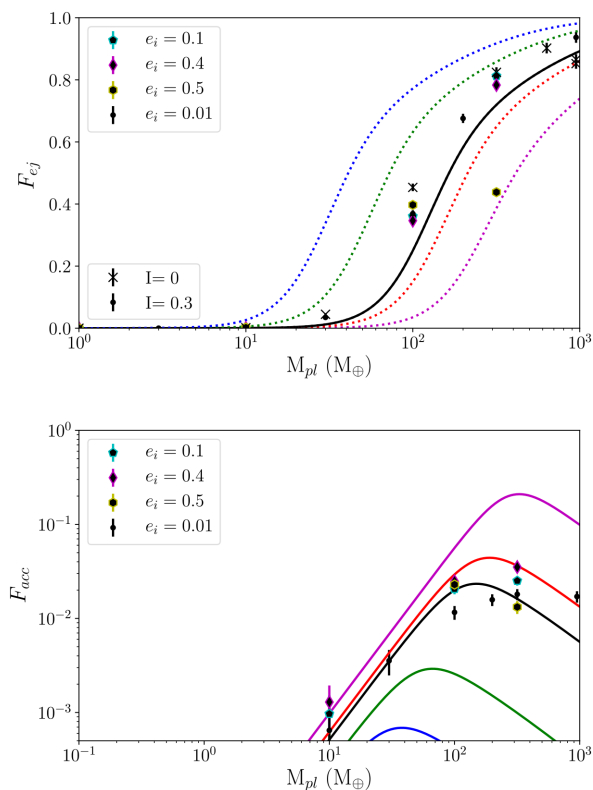


Figure A1. The same as the top panel of Figs 2 and 3 showing the results of the numerical simulations testing the effects of the initial particle eccentricity on the fraction of particles ejected and accreted as a function of planet mass, for $\beta = 0.1$, $a_{pl} = 1$ au and $e_i = 0.01, 0.1, 0.4, 0.5$. The solid lines show a fit to the results of the form equations (20) and (21), using the best-fitting parameters in Table 1. Error bars are 1σ , where $\sigma = \sqrt{N_{ej}/N}$.

Table A1. Table of variables.

Symbol	Units	Description
α_a		Parameter that describes dependence of accretion rate on planet mass
α_e		Parameter that describes dependence of ejection rate on planet mass
a_{pl}	au	Planet's semi-major axis
\dot{a}_{PR}	au yr ⁻¹	Rate of change of semi-major axis due to PR-drag
β		Ratio of radiative force to gravitational force from star
b_{ej}	au	Impact parameter for ejection
b_{acc}	au	Impact parameter for accretion
D	m	Particle diameter
Δt	s	Time for the particle to migrate past the planet
δ_a		Parameter that describes dependence of accretion rate on stellar mass
δ_e		Parameter that describes dependence of ejection rate on stellar mass
e_i		Particle's initial eccentricity
e		Particle's eccentricity when it interacts with the planet
ε		Parameter that describes decrease in fraction of particles ejected or accreted due to particles scattered inwards that migrate out of the planet's influence
F_{ej}		Fraction of particles ejected
F_{acc}		Fraction of particles accreted
F_{past}		Fraction of particles that migrate past the planet
γ_a		Parameter that describes dependence of accretion rate on planet semi-major axis
γ_e		Parameter that describes dependence of ejection rate on planet semi-major axis
K_{ej}		Constant of proportionality in ejection rate
K_{acc}		Constant of proportionality in accretion rate
I_i	Radians	Particle's initial inclination
I	Radians	Particle's inclination when it interacts with the planet
L_*	L_{\odot}	Stellar luminosity
M_{pl}	M_{\oplus}	Planet's mass
M_*	M_{\odot}	Stellar mass
n	m ⁻³	Number density of particles
N		Number of particles
N_{ej}		Number of particles ejected
N_{acc}		Number of particles accreted
η_a		Parameter that describes dependence of accretion rate on β
η_e		Parameter that describes dependence of ejection rate on β
Q_{PR}		Radiation pressure efficiency factor, assumed to be 1
ρ	kg m ⁻³	Particle density
ρ_{J}	kg m ⁻³	Jupiter's density
ρ_{pl}	kg m ⁻³	Planet density
R_{ej}		Rate of ejections
R_{acc}		Rate of accretions
R_{pl}	m	The planet radius
V_{tor}	m ³	Volume of torus occupied by particles
v_{rel}	ms ⁻¹	The relative velocity between the planet and particle
v_{pp}	ms ⁻¹	The velocity of the particle
v_{K}	ms ⁻¹	The Keplerian velocity of the planet
v_{esc}	ms ⁻¹	The escape velocity of the planet
μ		GM_*

Table A2. The results of the N -body simulations (see Section 2) for low initial inclinations ($I_i = 0\text{rad}$) and $M_* = 1M_\odot$.

β	a_{pl} (au)	M_{pl} M_\oplus	I_i (rad)	Ejected	Accreted	Total particles
0.010	1.0	1	0.0	0 ± 2	17 ± 4	3100
0.010	1.0	9	0.0	21 ± 4	61 ± 7	3100
0.010	1.0	30	0.0	207 ± 14	85 ± 9	3100
0.010	1.0	100	0.0	1654 ± 40	119 ± 10	3100
0.010	1.0	317	0.0	2514 ± 50	62 ± 7	3099
0.010	1.0	634	0.0	2720 ± 52	97 ± 9	3100
0.010	1.0	951	0.0	2628 ± 51	68 ± 8	3098
0.010	1.0	1585	0.0	2760 ± 52	4 ± 2	3100
0.010	1.0	3170	0.0	2955 ± 54	18 ± 4	3100
0.044	1.0	1	0.0	0 ± 2	25 ± 5	3100
0.044	1.0	3	0.0	0 ± 2	14 ± 3	3100
0.044	1.0	9	0.0	5 ± 2	24 ± 4	3100
0.044	1.0	30	0.0	223 ± 14	101 ± 10	3100
0.044	1.0	100	0.0	1157 ± 34	78 ± 8	3100
0.044	1.0	200	0.0	2212 ± 47	75 ± 8	3100
0.044	1.0	317	0.0	2655 ± 51	67 ± 8	3100
0.044	1.0	634	0.0	2754 ± 52	109 ± 10	3100
0.044	1.0	951	0.0	2665 ± 51	154 ± 12	3100
0.044	1.0	1585	0.0	2753 ± 52	52 ± 7	3100
0.044	1.0	3170	0.0	2940 ± 54	20 ± 4	3100
0.100	1.0	1	0.0	0 ± 2	8 ± 2	3100
0.100	1.0	9	0.0	5 ± 2	13 ± 3	3100
0.100	1.0	30	0.0	139 ± 11	49 ± 7	3100
0.100	1.0	100	0.0	1406 ± 37	64 ± 8	3100
0.100	1.0	317	0.0	2555 ± 50	47 ± 6	3100
0.100	1.0	634	0.0	2797 ± 52	62 ± 7	3100
0.100	1.0	951	0.0	2642 ± 51	269 ± 16	3100
0.100	1.0	951	0.0	2683 ± 51	234 ± 15	3100
0.100	1.0	1585	0.0	2737 ± 52	179 ± 13	3100
0.100	1.0	3170	0.0	2929 ± 54	59 ± 7	3100

Table A3. The results of the N -body simulations (see Section 2) for $a_{\text{pl}} = 1\text{au}$, $\beta = 0.1$ and $I_i = 0.3$, varying the stellar mass.

M_* M_\odot	M_{pl} M_\oplus	Ejected	Accreted	Total particles
0.010	100	3100 ± 55	0 ± 0	3100
0.100	100	3100 ± 55	0 ± 0	3100
2.000	100	121 ± 11	48 ± 6	3100
5.000	100	1 ± 1	33 ± 5	3100
0.010	1	1981 ± 44	8 ± 2	2310
0.100	1	85 ± 9	0 ± 0	3100
2.000	1	0 ± 0	0 ± 0	3100
5.000	1	0 ± 0	0 ± 0	3100

Table A4. The results of a sub-set of the N -body simulations (see Section 2), where initial eccentricities of the particles are varied.

β	a_{pl} (au)	M_{pl} M_{\oplus}	e_i (rad)	Ejected	Accreted
0.100	1	100	0.1	1118 \pm 33	64 \pm 8
0.100	1	10	0.1	0 \pm 0	3 \pm 1
0.100	1	1	0.1	0 \pm 0	0 \pm 0
0.100	1	317	0.1	2517 \pm 50	80 \pm 8
0.100	1	100	0.4	1074 \pm 32	77 \pm 8
0.100	1	10	0.4	2 \pm 1	4 \pm 2
0.100	1	1	0.4	0 \pm 0	0 \pm 0
0.100	1	317	0.4	2428 \pm 49	109 \pm 10
0.100	1	100	0.5	1231 \pm 35	71 \pm 8
0.100	1	10	0.5	6 \pm 2	1 \pm 1
0.100	1	1	0.5	0 \pm 0	0 \pm 0
0.100	1	317	0.5	1358 \pm 36	41 \pm 6

Table A5. The results of the N -body simulations (see Section 2). All simulations were for $M_* = 1M_{\odot}$ and $N = 3, 100$ particles and all those particles not ejected or accreted made it past the planet, except those marked by † where a single long-lived particle trapped in the 2:1 resonance exterior to the planet after 500Myr. Errors are $\frac{\sqrt{N}}{N}$ unless $N < 3$, in which case Poisson statistics from Gehrels (1986) are used.

β	a_{pl} (au)	M_{pl} M_{\oplus}	I_i (rad)	Ejected	Accreted
0.010	1.0	1	0.0	0 \pm 2	17 \pm 4
0.010	1.0	9	0.0	21 \pm 4	61 \pm 7
0.010	1.0	30	0.0	207 \pm 14	85 \pm 9
0.010	1.0	100	0.0	1654 \pm 40	119 \pm 10
0.010	1.0	317	0.0	2514 \pm 50	62 \pm 7
0.010	1.0	634	0.0	2720 \pm 52	97 \pm 9
0.010	1.0	951	0.0	2628 \pm 51	68 \pm 8
0.010	1.0	1585	0.0	2760 \pm 52	4 \pm 2
0.010	1.0	3170	0.0	2955 \pm 54	18 \pm 4
0.044	1.0	1	0.0	0 \pm 2	25 \pm 5
0.044	1.0	3	0.0	0 \pm 2	14 \pm 3
0.044	1.0	9	0.0	5 \pm 2	24 \pm 4
0.044	1.0	30	0.0	223 \pm 14	101 \pm 10
0.044	1.0	100	0.0	1157 \pm 34	78 \pm 8
0.044	1.0	200	0.0	2212 \pm 47	75 \pm 8
0.044	1.0	317	0.0	2655 \pm 51	67 \pm 8
0.044	1.0	634	0.0	2754 \pm 52	109 \pm 10
0.044	1.0	951	0.0	2665 \pm 51	154 \pm 12
0.044	1.0	1585	0.0	2753 \pm 52	52 \pm 7
0.044	1.0	3170	0.0	2940 \pm 54	20 \pm 4
0.100	1.0	1	0.0	0 \pm 2	8 \pm 2
0.100	1.0	9	0.0	5 \pm 2	13 \pm 3
0.100	1.0	30	0.0	139 \pm 11	49 \pm 7
0.100	1.0	100	0.0	1406 \pm 37	64 \pm 8
0.100	1.0	317	0.0	2555 \pm 50	47 \pm 6
0.100	1.0	634	0.0	2797 \pm 52	62 \pm 7
0.100	1.0	951	0.0	2642 \pm 51	269 \pm 16
0.100	1.0	951	0.0	2683 \pm 51	234 \pm 15
0.100	1.0	1585	0.0	2737 \pm 52	179 \pm 13
0.100	1.0	3170	0.0	2929 \pm 54	59 \pm 7
0.100	0.1	317	0.3	860 \pm 29	922 \pm 30
0.100	0.1	30	0.3	2 \pm 5	89 \pm 9
0.100	0.1	100	0.3	126 \pm 11	272 \pm 16
0.100	0.1	317	0.3	1320 \pm 36	547 \pm 23
0.100	0.1	634	0.3	2011 \pm 44	595 \pm 24
0.100	0.5	1	0.3	0 \pm 2	1 \pm 3
0.100	0.5	30	0.3	1 \pm 3	18 \pm 4
0.100	0.5	100	0.3	229 \pm 15	91 \pm 9
0.100	0.5	317	0.3	1766 \pm 42	100 \pm 10
0.002	1.0	30	0.3	417 \pm 20	243 \pm 15
0.002	1.0	100	0.3	2163 \pm 46	114 \pm 10
0.002	1.0	317	0.3	2747 \pm 52	112 \pm 10

Table A5 – continued

β	a_{pl} (au)	M_{pl} M_{\oplus}	I_i (rad)	Ejected	Accreted
0.005	1.0	30	0.3	287 ± 16	177 ± 13
0.005	1.0	100	0.3	1940 ± 44	131 ± 11
0.005	1.0	317	0.3	2639 ± 51	132 ± 11
0.010	1.0	1	0.3	0 ± 2	0 ± 2
0.010	1.0	9	0.3	7 ± 2	21 ± 4
0.010	1.0	30	0.3	241 ± 15	122 ± 11
0.010	1.0	100	0.3	1601 ± 40	132 ± 11
0.010	1.0	200	0.3	2354 ± 48	114 ± 10
0.010	1.0	317	0.3	2582 ± 50	110 ± 10†
0.010	1.0	951	0.3	2764 ± 52	80 ± 8†
0.044	1.0	1	0.3	0 ± 2	0 ± 2
0.044	1.0	9	0.3	0 ± 2	8 ± 2
0.044	1.0	30	0.3	177 ± 13	41 ± 6
0.044	1.0	100	0.3	1213 ± 34	85 ± 9
0.044	1.0	200	0.3	2244 ± 47	80 ± 8
0.044	1.0	317	0.3	2585 ± 50	79 ± 8
0.044	1.0	951	0.3	2767 ± 52	93 ± 9
0.044	1.0	1585	0.3	2818 ± 53	49 ± 7
0.044	1.0	3170	0.3	3064 ± 55	3 ± 1
0.100	1.0	1	0.3	0 ± 2	0 ± 2
0.100	1.0	3	0.3	0 ± 2	0 ± 2
0.100	1.0	9	0.3	0 ± 2	2 ± 3
0.100	1.0	30	0.3	108 ± 10	11 ± 3
0.100	1.0	100	0.3	1144 ± 33	36 ± 6
0.100	1.0	200	0.3	2095 ± 45	49 ± 7
0.100	1.0	317	0.3	2523 ± 50	56 ± 7
0.100	1.0	951	0.3	2904 ± 53	53 ± 7
0.100	1.0	1585	0.3	2960 ± 54	26 ± 5
0.400	1.0	1	0.3	0 ± 2	0 ± 2
0.400	1.0	100	0.3	91 ± 9	9 ± 3
0.400	1.0	317	0.3	1438 ± 37	16 ± 4
0.100	10.0	1	0.3	0 ± 2	0 ± 2
0.100	10.0	30	0.3	634 ± 25	4 ± 2
0.100	10.0	100	0.3	2038 ± 45	9 ± 3
0.100	10.0	317	0.3	2916 ± 54	12 ± 3
0.100	50.0	1	0.3	1 ± 3	0 ± 2
0.100	50.0	30	0.3	1070 ± 32	0 ± 2
0.100	50.0	100	0.3	2516 ± 50	3 ± 1

This paper has been typeset from a $\text{\TeX}/\text{\LaTeX}$ file prepared by the author.